Influence of aerosols and surface reflectance on satellite NO_2 retrieval: Seasonal and spatial characteristics and implications for NO_x emission constraints

J.-T. Lin [1], M.-Y. Liu [1], J.-Y. Xin [2], K. F. Boersma [3,4], R. Spurr [5], R. Martin [6,7], Q. Zhang [8]

[1] Laboratory for Climate and Ocean-Atmosphere Studies, Department of Atmospheric and Oceanic Sciences, School of Physics, Peking University, Beijing 100871, China

[2] State Key Laboratory of Atmospheric Boundary Layer Physics and Atmospheric Chemistry, Institute of Atmospheric Physics, Chinese Academy of Sciences, Beijing, 100029, PR China

[3] Royal Netherlands Meteorological Institute, De Bilt, The Netherlands

[4] Meteorology and Air Quality department, Wageningen University, Wageningen, the Netherlands.

[5] RT Solutions Inc., Cambridge MA 02138, USA

[6] Department of Physics and Atmospheric Science, Dalhousie University, Halifax, Nova Scotia, Canada

[7] Atomic and Molecular Physics Division, Harvard‐Smithsonian Center for Astrophysics, Cambridge, Massachusetts, USA

[8] Ministry of Education Key Laboratory for Earth System Modeling, Center for Earth System Science, Tsinghua University, Beijing, China

Correspondence: J.-T. Lin (linjt@pku.edu.cn)

Short title: Aerosol and surface reflectance affect NO_2 retrieval

Abstract

Satellite retrievals of vertical column densities (VCDs) of tropospheric nitrogen dioxide (NO_2) normally do not explicitly account for aerosol optical effects and surface reflectance anisotropy that vary with space and time. Here, we conduct an improved retrieval of NO_2 VCDs over China, called the POMINO algorithm, based on measurements from the Ozone Monitoring Instrument (OMI), and we test the importance of a number of aerosol and surface reflectance treatments in this algorithm. POMINO uses a parallelized LIDORT-driven AMFv6 package to derive tropospheric air mass factors via pixel-specific radiative transfer calculations with no look-up tables, taking slant column densities from DOMINO v2. Prerequisite cloud optical properties are derived from a dedicated cloud retrieval process that is fully consistent with the main NO_2 retrieval. Aerosol optical properties are taken from GEOS-Chem simulations constrained by MODIS AOD values. MODIS bi-directional reflectance

distribution function (BRDF) data are used for surface reflectance over land. For the present analysis, POMINO level-2 data for 2012 are aggregated into monthly means on a 0.25 °long. x 0.25 °lat. grid.

POMINO-retrieved annual mean NO_2 VCDs vary from 15–25 x 10^{15} cm^{-2} over the polluted North China Plain (NCP) to below 10^{15} cm^{-2} over much of west China. Using POMINO to infer Chinese emissions of nitrogen oxides leads to annual anthropogenic emissions of 9.05 TgN yr^{-1}, an increase from 2006 (Lin, 2012) by about 19%. Replacing the MODIS BRDF data with the OMLER v1 monthly climatological albedo data affects NO_2 VCDs by up to 40% for certain locations and seasons. The effect on constrained NO_x emissions is small. Excluding aerosol information from the retrieval process (this is the traditional "implicit" treatment) enhances annual mean NO_2 VCDs by 15–40% over much of east China. Seasonally, NO_2 VCDs are reduced by 10–20% over parts of the NCP in spring and over north China in winter, despite the general enhancements in summer and fall. The effect on subsequently-constrained annual emissions is between -5% and +30% with large seasonal and spatial dependence. The implicit aerosol treatment also tends to exclude days with high pollution, since aerosols are interpreted as effective clouds and the respective pixels are often excluded by cloud screening; this is a potentially important sampling bias. Therefore an explicit treatment of aerosols is important for space-based NO_2 retrievals and emission constraints. A comprehensive independent measurement network with sufficient spatial and temporal representativeness is needed to further evaluate the different satellite retrieval approaches.

1. Introduction

Tropospheric nitrogen oxides (NO_x = NO + NO_2) are important pollutants affecting ozone, aerosols, acid deposition, and climate. China has become the top emitter of NO_x due to its recent anthropogenic emission growth along with reductions in North America and Europe (Richter et al., 2005; van der A et al., 2008; Zhang et al., 2009; Lamsal et al., 2011; Castellanos and Boersma, 2012; Lin et al., 2014a). High NO_x pollution not only has significant consequences for China's domestic environment (Zhao et al., 2009; Lin et al., 2010a; Zhang et al., 2012), but it has also raised concerns regarding long-range pollution transport to downstream regions (Lin et al., 2008; Cooper et al., 2010; Lin et al., 2014a; Zhang et al., 2014; Jiang et al., 2015).

Vertical column densities (VCDs) of tropospheric nitrogen dioxide (NO_2) retrieved from the Ozone Monitoring Instrument (OMI) have been used extensively to study Chinese NO_x pollution (Stavrakou et al., 2008; Zhao and Wang, 2009; Lin et al., 2010b; Mijling et al., 2013; Miyazaki and Eskes, 2013). The high spatiotemporal coverage of OMI is superior to ground-based in situ measurements. However, NO_2 retrievals from OMI and other space-borne instruments are subject to large systematic and random errors due to uncertainties in the conversion process from radiance to VCDs (Boersma et al., 2011; Bucsela et al., 2013). In particular, current NO_2 algorithms take an implicit approach to accounting for aerosol optical effects, with no

explicit specification of aerosols in the retrievals of both NO_2 VCDs and ancillary cloud parameters. The rationales for this approach are (1) aerosols affect the retrieval of cloud parameters, so that the retrieved cloud parameters are "effective" and implicitly contain certain aerosol information, and (2) these effective cloud parameters at least partly describe the effect of aerosols on NO_2 air mass factors (Boersma et al., 2004; Boersma et al., 2011). This implicit treatment is supported by the good spatial correlation (0.66) observed between coincident MODIS aerosol optical thickness values (mostly due to scattering) and O_2-O_2 effective cloud fractions over the eastern United States (Boersma et al., 2011).

Our previous study (Lin et al., 2014b) for several locations in the North China Plain (NCP) has shown large changes in retrieved NO_2 VCDs when moving from an implicit to an explicit treatment of aerosols. In particular, NO_2 VCDs are reduced by 14% on average but are changed by (-90)–(+70)% for individual pixels when aerosol optical depth (AOD) exceeds 0.8. In addition, current NO_2 retrievals are often based on monthly climatological surface albedo data, not accounting for the angular dependence of surface reflectance and its interannual variability; the corresponding effect on retrieved NO_2 has been estimated at 0–20% for Europe (Zhou et al., 2010) and the NCP (Lin et al., 2014b) on average. Despite the complex terrains (Fig. 1a), complex land use types (Fig. 1b), and high aerosol loadings (Xin et al., 2007; Che et al., 2009; Wang et al., 2011) over China, the effects of aerosol and surface reflectance treatments are largely unknown.

This study extends our previous work (for a few locations; Lin et al., 2014b) to introduce an improved pixel-specific level-2 retrieval of tropospheric NO_2 VCDs over China (80 °E–130 °E, 20 °N–53 °N), Peking University OMI NO_2 (POMINO). Using a parallelized LIDORT-driven AMFv6 package (Palmer et al., 2001; Martin et al., 2003; Lin et al., 2014b), we explicitly account for aerosol optical effects, surface reflectance anisotropy, and their spatiotemporal variability. We then evaluate the individual and combined effects of an implicit aerosol treatment and changes in surface reflectance characteristics. In particular, we show large seasonal and spatial dependence of the effects of aerosol and/or surface reflectance treatments. We further illustrate the influences on subsequent NO_x emission constraints, a popular application of OMI data. Our POMINO data are available for 2004–2013 and will be updated to more recent times. Results for 2012 are presented here, by aggregating level-2 data into monthly mean values on a 0.25 ° long. x 0.25 ° lat. grid. Various provinces and regions are defined in Fig. 1a to facilitate the present analysis.

Section 2 presents our POMINO retrieval approach. Section 3 analyzes the POMINO NO_2 VCDs and the effects of various treatments of aerosols and surface reflectance. Section 4 further shows the effects on subsequent NO_x emission constraints. Section 5 concludes the present study with a further discussion on the applicability of our POMINO approach for a fast global retrieval from future fine-resolution satellite instruments.

2. Methodology

2.1 General process to retrieve tropospheric NO_2 VCDs

The OMI is a nadir-viewing imaging spectrometer onboard the polar-orbiting Sun-synchronous EOS Aura satellite with an equator crossing time at 13:45 (Levelt et al., 2006). For each of the 14 or 15 orbits per day, the sensor measures UV-Visible radiation reflected by the Earth from 60 across-track pixels with a swath of 2600 km. The pixel size is small and varies with the viewing angle (from 13 km x 24 km at nadir to 25 km x 150 km at the swath edge). The OMI pixels cover the globe on a daily basis, but the coverage of valid data is reduced by cloud and snow/ice contamination and by recent row anomaly issues (especially since 2009). Row anomaly affects the quality of the level 1B radiance data for some viewing directions of OMI (http://www.knmi.nl/omi/research/product/rowanomaly-background.php).

Retrieval of tropospheric NO_2 VCDs from satellite normally undergoes a three-step process (Boersma et al., 2011). The first step derives slant column densities (SCDs) from satellite radiance data, and the second step separates the contribution of the tropospheric from the stratospheric part of the SCD. The final step involves an air mass factor (AMF) calculation to derive tropospheric VCDs (i.e., VCD = SCD / AMF). The AMF calculation is affected by surface reflectance, aerosol optical effects, cloud fraction (CF), cloud top pressure (CP), and atmospheric profiles of pressure, temperature and NO_2 (Zhou et al., 2010; Boersma et al., 2011; Bucsela et al., 2013; Lin et al., 2014b). Accurate knowledge of these parameters is an important prerequisite to the NO_2 retrieval. Over polluted regions like many parts of China, the AMF calculation is the dominant error source for retrieved tropospheric NO_2 data. Hereafter, SCDs, VCDs and AMFs are referred to as their tropospheric portions.

Before the main NO_2 retrieval itself, CF and CP are normally retrieved with the O_2-O_2 approach (Acarreta et al., 2004). Here, clouds are treated simply as an isotropically reflecting surface at a certain level (CP) with a Lambertian albedo of 0.8. As such, cloud optical properties are constrained by the two parameters CF and CP that can be retrieved from OMI data. Although O_2-O_2 cloud parameters are retrieved in a consistent manner with the latest DOMINO v2 NO_2 retrievals (same surface albedo assumption, same radiative transfer model, same cloud model; Boersma et al. (2011)) to ensure that the effective radiative properties of the scene are consistent between the cloud and NO_2 retrievals, some inconsistencies have recently come to light with respect to different atmospheric pressure and temperature profiles and terrain heights (Maasakkers, 2013; Lin et al., 2014b).

2.2 Our POMINO retrieval approach

In this paper, our POMINO algorithm, referred to as case REF, largely follows the method described by Lin et al. (2014b) with a few modifications. Here we present a brief summary of the algorithm, placing emphasis on the latest modifications. The

reader is referred to Lin et al. (2014b) for a detailed description. Our retrieval is focused on the derivation of tropospheric AMFs to calculate tropospheric VCDs, taking the tropospheric SCD data (Dirksen et al., 2011) from DOMINO v2 (Boersma et al., 2011). We adjust the calculated layer AMFs to correct for the temperature dependence of NO_2 absorption cross section that is not accounted for in the SCD data (Boersma et al., 2004). Following Lin et al. (2014b), we re-retrieve the prerequisite (O_2-O_2 based) cloud properties by using a set of parameters consistent with those in the retrieval of NO_2. Our cloud retrieval is focused on AMF calculations, starting with the O_2-O_2 SCDs from the official cloud product OMCLDO2 v3 (Acarreta et al., 2004). Table 1 summarizes our retrieval approach and parameters. Figure 2 briefly illustrates the retrieval procedure.

We calculated the AMFs for O_2-O_2 (to derive CF and CP; at 475 nm) and NO_2 (at 438 nm) by using a newly improved AMFv6 package (Palmer et al., 2001; Martin et al., 2003; Lin et al., 2014b) to coordinate the retrieval process. The AMFv6 code makes use of the LIDORT v3.6 radiative transfer model (RTM) (Spurr, 2008). Explicit radiative transfer is calculated pixel by pixel. Both the AMFv6 and LIDORT v3.6 codes have been parallelized via OpenMP. The parallelization has little overhead, in that, by using 16 computational cores in parallel, the speed-up is close to a factor of 16 relative to the single-core performance. With this speedup, a pixel-specific radiative transfer calculation becomes feasible for a large-scale (large domain, long time) retrieval, as in the present study. The traditional use of a look-up table to interpolate the AMFs is then no longer needed.

We used data for vertical profiles of NO_2, pressure and temperature on a relatively high-resolution grid (0.667 ° long. x 0.5 ° lat.). The NO_2 data were simulated by the GEOS-Chem chemical transport model (CTM), and pressure and temperature data were taken from the GEOS-5 assimilated meteorological fields that were used to drive GEOS-Chem simulations. GEOS-Chem has been shown to capture vertical profiles of NO_2 and ozone over the United States from aircraft measurements (Lin and McElroy, 2010). Appendix A summarizes the CTM simulations. As we retrieve clouds and NO_2 pixel by pixel, model information at the grid cell covering the pixel center is used. Although the size of our model grid cell is larger than the size of an OMI pixel, our model grid cell size is much smaller than used in other OMI products (3 ° long. x 2 ° lat. for DOMINO [Boersma et al., 2011] and 2.5 ° long. x 2 ° lat. for OMNO2 [Bucsela et al., 2013]). In addition, we adjust the pressure profile based on the difference between pixel-specific surface elevation and grid cell average elevation (Zhou et al., 2009; Lin et al., 2014b). The meteorological and particularly NO_2 profiles are subject to errors (Boersma et al., 2011; Lin et al., 2014b). Further research is needed to evaluate these profiles using available measurements over China.

Our retrieval explicitly accounts for the effects of spatiotemporally varying aerosols and surface reflectance anisotropy on radiation. These two factors have proved relevant for the NO_2 retrieval (Zhou et al., 2010; Lin et al., 2014b; Noguchi et al., 2014). Detailed information is presented in Sects. 2.4 and 2.5.

2.3 Pixel selection, pixel-to-grid conversion, and sensitivity retrievals

For our present analysis, an OMI pixel is selected only when the ground is free from snow and ice, and when the CRF does not exceed 50% (Boersma et al., 2011; Lin et al., 2014b). Pixels with row-anomaly contamination are discarded. Data from valid pixels are then converted to monthly mean values on a 0.25 ° long. x 0.25 ° lat. grid through an area-weighted interpolation process. This process has been applied to NO_2 and all associated parameters. Section 3.5 discusses the number of days per month with valid pixels on the gridded map.

In addition to our POMINO retrieval (case REF), three other retrievals (cases SRF, AER, and S_A) were performed to evaluate the sensitivity of retrieved NO_2 VCDs and associated cloud parameters to changes in aerosols and surface reflectance. These additional retrievals, together with the standard DOMINO v2 product (referred to as case DOM) (Boersma et al., 2011), were compared with case REF. These tests are summarized in Table 2.

There are notable differences in the representation of CRF between POMINO and DOMINO. For POMINO, the CRF represents the fraction of the TOA radiance caused by clouds alone (in the context of additional contributions from the surface and aerosols). For DOMINO, however, the CRF applies to the fraction of TOA radiance caused by both clouds and aerosols, with surface reflectance represented by a geometry-independent surface albedo.

Different retrieval approaches lead to distinctive CRF values, which in turn has consequences for the selection of valid data (Lin et al., 2014b) (see discussions in Sect. 3.5). In Sects. 2 and 3, the pixels designated as "valid" by case REF are selected for analysis, regardless of their validity status in other retrievals. This choice ensures that the same set of pixels is evaluated for all retrieval methods. For the emission constraint study in Sect. 4, different sets of valid pixels specific to the individual retrieval approaches are also analyzed, in addition to the set determined by case REF.

2.4 Surface reflectance in POMINO (case REF)

Accurate knowledge of surface reflectance is of key importance for retrievals of NO_2 and ancillary cloud parameters. Surface reflectance depends both on the ground conditions and on the state of the overlaying atmosphere (the latter determining the relative amounts of diffuse versus direct incident radiance) (Lucht et al., 2000). Due to inhomogeneity in surface conditions, the amount of reflected radiance relative to a given amount of incident radiance depends on the incoming and outgoing angles. The degree of angular dependence is determined by surface roughness and vegetation characteristics (type, leaf area, and geometric shape). The angular dependence is most prominent for direct incident radiance; angular effects on the reflected radiation field are largely cancelled out for diffuse (isotropic) incident radiance (Lucht et al., 2000). Normally the angular dependence is not accounted for in the NO_2 retrievals, with a

few exceptions, e.g., Zhou et al. (2010) for Europe, Noguchi et al. (2014) for Tokyo, and Lin et al. (2014b) for several locations in China.

Case REF explicitly accounts for the angular dependence of surface reflectance. It adopts the MODIS BRDF product as approximate realization of the complex dependence of surface reflectance to radiation geometry (Lucht et al., 2000). This product is based on BRDF models using a linear combination of three near-independent reflecting kernels: isotropic (no angular dependence), volumetric (related to leaf area), and geometric (related to vegetation shape). Each kernel contribution is regulated by a parameter that varies with time and space. We used the snow- and ice-free MCD43C2 Collection 5 dataset (Lucht et al., 2000) that provides the kernel parameters at 440 nm as 16 day average values on a 0.05 ° long. x 0.05 ° lat. grid. Kernel parameters are updated every eight days, accounting for the seasonal and interannual variability in BRDF. To cover missing values and reduce noise, the high-resolution data were passed through a spatiotemporal interpolation and smoothing procedure. The data were then mapped to each OMI pixel for subsequent AMF calculations. A detailed description of these customized procedures is presented in Lin et al. (2014b). Figures S1a-S1c present the horizontal distributions of BRDF kernel parameters on the original 0.05 ° long. x 0.05 ° lat. grid for the time period of June 25th, 2012–July 10th, 2012.

Over China, the angular dependence of surface reflectance is more important over parts of the west, southwest, southeast and northeast having complex terrains (Fig. 1a), vegetated lands (Fig. 1b), and relatively low aerosol loadings (Fig. 3, first row). Over the NCP and many other polluted regions of China, high aerosol loadings (Fig. 3, first row) mean that most incident radiation to the ground is diffuse, so that the angular dependence is reduced for the radiance reflected from the ground. Nonetheless, the seasonal and interannual variability in surface reflectance may still be important for China, especially considering rapid land use change due to urbanization, industrialization and agricultural activities (Liu et al., 2014).

Over the oceans, there are no applicable BRDF data; therefore, we used the surface albedo data from the OMLER v3 product on a 0.5 ° long. x 0.5 ° lat. grid (Kleipool et al., 2008). This albedo dataset is a 5-year (2005–2009) mean monthly climatology, an update of OMLER v1 adopted by DOMINO v2. The oceanic pixels are included for completeness in our product; exclusion or inclusion of these pixels has little effect on our present analysis. Figure S1d shows the OMLER v3 data in July.

Figure 4 (first row) presents the horizontal distribution of annual and seasonal bi-directional reflectance factor (BRF) values in 2012, as representative of MODIS BRDF, over land and OMLER v3 albedo over the ocean. The data have been sampled from valid OMI pixels and mapped to a 0.25 ° long. x 0.25 ° lat. grid, as described in Sect. 2.3. The BRF here is the ratio of reflected radiance to the π-divided direct incident irradiance (along the geometric light path from the Sun to the ground and then to the OMI) (Schaepman-Strub et al., 2006). Especially for incident radiation

with strong direct and weak diffuse contributions, the value of BRF is critical for the total amount of radiation received by OMI. The BRF data in Fig. 4 (first row) imply that the spatial and temporal variations in solar zenith angle are taken into account, in addition to changes in the ground characteristics. The choice of BRF for presentation purposes follows Zhou et al. (2010) and Lin et al. (2014b).

Figure 4 (first row) shows that in all seasons, the BRF reaches maximum values of 0.1–0.3 over west and northwest China with desert or bare land. The minimum values at 0.02–0.04 occur in parts of east China where there is stronger absorption by vegetation (Fig. 1b). Especially over east China, the relatively high (low) BRF values are often coincident with high (low) AOD (comparing Figs. 3 and 4, first rows), likely indicating the presence of aerosol contamination in the BRDF data. The BRF data exhibit significant seasonal variation. Over east China, the BRF often reaches maximum values in summer and minima in fall. For example, over much of the NCP, the BRF varies from 0.06–0.08 in summer to 0.04–0.06 in fall. Over the west, the summer season has the lowest BRF values, likely a result of lower solar zenith angle.

2.5 Aerosol optical properties in POMINO (case REF)

POMINO explicitly accounts for the optical effects of aerosols, given the high aerosol loadings over China (Fig. 3, first row). Lin et al. (2014b) has a detailed description of the implementation of aerosol optical properties in the retrieval process. Here we emphasize the modifications to POMINO needed to facilitate a large-scale retrieval (i.e., for a large domain in all seasons, as compared to several spot-locations investigated by Lin et al. (2014b)).

Day-to-day varying aerosol optical properties (AOD, single scattering albedo (SSA), phase functions, and vertical profiles) are taken from the GEOS-Chem v9-02 simulations on a 0.667 ° long. x 0.5 ° lat. grid. The model is updated from an earlier version v8-03-02 used by Lin et al. (2014b). See Appendix A for model descriptions. GEOS-Chem simulates various aerosol types, including secondary inorganic aerosols (sulfates, nitrates, and ammoniums), organic aerosols, black carbon, dust and sea salts. For a given OMI pixel, aerosol data at the grid cell covering the pixel center are used during the retrieval process. Aerosol optical properties at two wavelengths are implemented to retrieve NO_2 (438 nm) and clouds (475 nm), respectively.

To constrain the AOD, CTM-modeled AOD at 550 nm are adjusted to match MODIS/Aqua data on a monthly basis (Appendix B). The AOD adjustment is then carried over to other wavelengths (438 nm and 475 nm) based on species-specific size distributions, refractive indices and hygroscopic growth rates as assumed in GEOS-Chem. The same procedure was used in Lin et al. (2014b).

Figure 3 (first row) presents the horizontal distribution of AOD at 550 nm used in POMINO. Both annual and seasonal mean data are shown. High AOD values are apparent over the NCP (annual mean = 0.8–1.0), the Sichuan Basin (0.8–1.0), and

parts of south China (0.6–0.8) due to significant anthropogenic sources. The high AOD values over the Sichuan Basin are also a result of long-lasting stagnant atmosphere. Large AOD values are also present over the western deserts, especially in spring (0.9–1.2), which has the highest dust emissions. Over east China, AOD values are higher in spring and summer than in fall and winter. These spatial and temporal patterns are generally consistent with previous findings (Xia et al., 2007; Xin et al., 2007; Wang et al., 2011; Lin et al., 2014c).

Figure 3 (second row) shows the SSA at 550 nm. The SSA is largest over west and northwest China, where there are few black carbon sources. Over the west, the SSA varies between 0.92 and 0.98 in all non-winter seasons. In winter, the SSA is reduced to 0.90–0.92 over large parts of Xinjiang. Over east China, the SSA experiences even larger seasonal and spatial variability, from ~ 0.80 over parts of the NCP in winter to 0.94–0.96 over most of east China in summer. The seasonality of SSA is mostly a consequence of black carbon emissions reaching their maximum values in winter and minimum amounts in summer (see Appendix A for the implementation in GEOS-Chem).

Figure 3 (second row, filled circles) shows SSA values for 2005 estimated by Lee et al. (2007) from MODIS top-of-atmosphere radiance and ground AOD networks. Their estimates are only for situations with AOD > 0.4, and have a root mean square error of 0.03. Differences between our SSA values and Lee et al. are highly season- and location-dependent. On a seasonal basis, our SSA values, sampled at grid cells covering their sites, are most consistent with Lee et al. in winter (mean difference across China = -0.02±0.05), followed by spring, summer and fall. Note that these comparisons are qualitative, given the inconsistency in data sampling.

Several limitations constrain our ability to improve aerosol modeling. Model aerosol optical properties (AOD, SSA, phase functions) and vertical profiles are subject to errors (Drury et al., 2010; Ford and Heald, 2012; van Donkelaar et al., 2013). We used MODIS AOD data to constrain CTM-derived AOD, even though MODIS data are not free of errors (Wang et al., 2007; Wang et al., 2010; Hyer et al., 2011). No adequate observations are available to constrain other aerosol optical parameters at a regional scale with high spatial and temporal resolutions. Observation-based estimates of SSA are essentially lacking at the scale considered here, and the few results in the literature contain large uncertainties (±0.03) (Lee et al., 2007). Although the CALIOP instrument provides information of aerosol vertical profiles (Winker et al., 2009), the CALIOP profiles are limited by their spatiotemporal coverage and data quality (especially near the ground) (Ford and Heald, 2012; van Donkelaar et al., 2013). Note that since the same vertical mixing and convection schemes were used to simulate aerosols and NO_2, the height of aerosols relative to NO_2 (above or below or mixed with NO2 relevant to our study) may be subject to smaller errors than the absolute height of aerosols. Therefore we expect certain errors in aerosol optical properties that may affect the accuracy of our present NO_2 retrieval. Future work is needed to better understand and constrain aerosol properties.

Nevertheless, our present study, at the very least, reveals the importance of an explicit aerosol treatment for NO_2 and associated cloud-parameter retrievals at a regional scale, especially given the lack of such an explicit treatment in current satellite products. In support of our work here, Lin et al. (2014b) showed that, by explicitly accounting for aerosols with just the AOD values constrained by observations, there is excellent correlation between retrieved NO_2 VCDs and independent MAX-DOAS data (R^2 = 0.96 in day-to-day variability across the few locations being studied). Section 3.3 further shows large changes in retrieved NO_2 VCDs from an explicit to an implicit treatment of aerosols, and Sect. 4 illustrates the consequences on subsequent NO_x emission constraint. Therefore, we expect that the explicit inclusion of aerosols will improve the NO_2 retrieval, especially if more comprehensive observations become available to constrain model aerosols.

3. OMI NO_2 retrievals and complex influences of aerosols and surface reflectance

3.1 General characteristics of POMINO NO_2 (case REF)

Figure 5 (first row) shows annual and seasonal mean NO_2 VCDs from POMINO (case REF) on a 0.25 ° long. x 0.25 ° lat. grid. At this fine resolution, hotspots of NO_2 pollution across China are clearly visible. The formation of hotspots is also a result of the short lifetime of NO_2 (2–3 hours to 1 day, depending on chemical activity). Large pollution covers over much of the NCP, with annual mean NO_2 VCDs exceeding 15 x 10^{15} cm^{-2}, due to emissions from both urban and regional sources. Annual mean NO_2 VCDs are below 10^{15} cm^{-2} over much of west China due to lack of anthropogenic influences. The spatial gradient of NO_2 pollution is greatest in summer due to its shortest lifetime, but the NCP still has a large inter-connected area of high NO_2. This regional-scale high pollution highlights the severity and extensiveness of China's environmental problems.

Figure 5 (first row) also shows a large seasonal variation in NO_2. Over east China, NO_2 VCDs reach maxima in winter and minima in summer. The maximum to minimum ratio is about 3.6 for all regions east of 101.25 °E. The large seasonality in NO_2 VCDs mainly reflects the seasonality in the species' lifetime (Lin, 2012). Over most of west China with few anthropogenic emissions, NO_2 VCDs are largest in summer due to a peak in natural (lightning and soil) sources that overcompensates for the shortest lifetime. This seasonal pattern is most notable over Tibet and Qinghai. For west China (west of 101.25 °E) as a whole, the ratio of summer peak to winter minimum is about 1.4. Over much of Xinjiang and Inner-Mongolia, the growth in anthropogenic influences has meant a winter maximum and a summer minimum, reversing the seasonality typical for west China.

Figure 5 (fifth row) presents the difference in NO_2 VCDs between the cases DOM and REF, as a percentage fraction of REF. Case DOM is taken from DOMINO v2 (Boersma et al., 2011) and sampled from pixels valid in case REF, irrespective of whether these pixels are flagged as valid in the DOMINO v2 product. (Note that in

Sect. 4, valid pixels from case REF and DOMINO v2 are both evaluated for the derivation of NO_x emissions.) Figure 5 (fifth row, first panel) shows that at an annual scale, results from case DOM exceed those from REF by 0–60% over central east China (consistent with POMINO NO_2 columns being ~45% lower than DOMINO, as reported in Lin et al. [2014]) and much of the west. Case DOM results are smaller than those from REF over parts of the south and north. Seasonal dependence is significant (Fig. 5, fifth row). Over the NCP, case DOM is greater than REF by 10–40% in summer, while the signs of difference are location-dependent in winter. Over most of Tibet, case DOM is similar to REF in the fall season, but greatly exceeds REF (by up to 40%) in other seasons. These differences reflect the dissimilar AMF approaches in the two retrievals. It is beyond the scope of this study to fully elucidate the differences between case REF (POMINO) and DOMINO v2. Instead, the following sections analyze the effects of surface reflectance and aerosols on retrieved NO_2 VCDs.

3.2 Effects of surface reflectance on NO_2 and cloud retrievals

The MODIS BRDF data account for spatial and temporal variability in surface reflectance as well as its angular dependence. Here we evaluate the sensitivity of retrieved NO_2 VCDs to surface reflectance, by adopting an alternate surface reflectance dataset to repeat the retrieval process.

Case SRF adopts the OMI monthly climatological albedo data (OMLER v1, at 440 nm) from the DOMINO v2 product and re-derives cloud properties and NO_2 VCDs; other retrieval procedures, including aerosol treatments, are unchanged. Unlike the MODIS BRDF, the OMI albedo data are monthly climatology (October 2004–October 2007 average) with no interannual variability. The OMI albedo dataset means isotropic reflectance with no angular dependence. The horizontal resolution of OMI albedo data is 0.5 ° long. x 0.5 ° lat., compared to the high-resolution MODIS BRDF data (at 0.05 ° long. x 0.05 ° lat.). The use of OMI albedo data tests the sensitivity of retrieved NO_2 to large changes in surface reflectance.

Figure 4 (second row) compares the OMI albedo with the MODIS BRF over China. The OMI albedo is normally within ±0.05 of the MODIS BRF. Over most of east China, the OMI albedo exceeds the MODIS BRF in all seasons with a difference of 0.01–0.04. Over northeast China, however, the OMI albedo is lower than the MODIS BRF in spring and winter. Over most of west China, the OMI albedo is smaller than the MODIS BRF with a difference of 0.01–0.06. The OMI albedo greatly exceeds the MODIS BRF at various locations in the west and north (by 0.10 or more).

The diagram in Fig. 6 illustrates how a change in surface reflectance affects the pre-NO_2 cloud retrieval. In the cloud-property O_2-O_2 algorithm, higher reflectance leads to lower effective CF, since fewer clouds are needed to reflect a given amount of radiation to the outer space. Effects of changing surface reflectance on CP are multifold. Higher reflectance means an enhanced AMF in the clear-sky portion of the

OMI pixel (AMFcr), which can be compensated by a decrease in CP. In addition, the reduction in CF caused by enhanced surface reflectance has a secondary effect on CP. A decrease in CF may lead to a further reduction in CP if the AMF of O_2-O_2 in the cloudy portion of the OMI pixel, AMFcl, is smaller than AMFcr (this is a "screening" effect of clouds on radiation). This effect occurs in most situations where the cloud top is distant from the ground and there is alow above-cloud O_2-O_2 concentration. Occasionally, a decrease in CF may result in an enhancement in CP, when the cloud top is close to the ground and thus the value of AMFcl exceeds AMFcr (an "albedo" effect of clouds on radiation).

Figure 7 contrasts case REF and SRF for the CF, cloud radiance fraction (CRF) and CP at an annual scale. A negative correlation is apparent between changes in CF (and CRF) from case REF to SRF and changes in surface reflectance. Over land, the CP tends to change in the opposite direction to the change in surface reflectance. Over much of the oceans away from Chinese coasts, however, the CP decreases with declining surface reflectance from case REF to SRF; this is due to the "albedo" effect of clouds (CP = 800–900 hPa). Overall, the CP changes from case REF to SRF with an opposite sign as surface reflectance for about 78% of all grid cells and months. Changes are similar across different seasons for individual cloud parameters (Figs. S2–S4, second rows).

As shown in Eq. 1 (the IPA or Independent Pixel Approximation), changes in CRF affect the relative weights of NO_2 AMFcl versus AMFcr, while changes in CP affect the absolute magnitude of NO_2 AMFcl. In addition, an increase in surface reflectance results in an enhancement in NO_2 AMFcr. These factors together determine the effects of surface reflectance on the NO_2 retrieval.

$$AMF = AMFcl \cdot CRF + AMFcr \cdot (1 - CRF) \qquad (1)$$

$$VCD = \frac{1}{1/VCDcl \cdot CRF + 1/VCDcr \cdot (1 - CRF)} \qquad (2)$$

Figure 5 (second row) shows that the effects of surface reflectance on retrieved NO_2 VCDs are largely region- and season-dependent. Over most Chinese regions except central and southeast China, replacing the MODIS BRDF with OMI albedo tends to increase the retrieved NO_2 VCDs by 0–40% (mostly less than 15%). Over central and southeast China, however, the use of OMI albedo reduces NO_2 VCDs by 0–20% in spring, fall and winter but with a slight enhancement in summer. This spatial and seasonal divergence in NO_2 changes reflects the complex influences of surface reflectance on retrieved cloud properties and NO_2 AMFs. The magnitude of NO_2 changes is comparable to previous studies (Zhou et al., 2010; Lin et al., 2014b).

Figures 8b presents the percentage changes in NO_2 VCDs from case REF to SRF as a

function of AOD values (binned at intervals of 0.05) and changes in surface reflectance (i.e., OMI albedo minus MODIS BRF, binned at intervals of 0.01). Here the percentage changes from all grid cells and months with respect to each bin of AOD and surface reflectance change are averaged; the frequency of data located in each bin is shown in Fig. 8a. Figures 8c and 8d also separate the effects of surface reflectance on NO_2 VCDs for the pixel clear-sky and cloudy portions. Here, a clear-sky VCD (VCDcr) is derived as the SCD divided by AMFcr, and a cloudy-sky VCD (VCDcl) represents the SCD divided by AMFcl; Equation (2) shows the relation between VCD, VCDcr and VCDcl. Pixels with no clouds are excluded from calculations of AMFcl and VCDcl. The VCDcr and VCDcl for individual pixels are aggregated to respective monthly mean values in the same way as was done for the total VCD.

Figure 8c shows that, when the OMI albedo is larger (smaller) than the MODIS BRF, we get a reduction (enhancement) in VCDcr. The relative changes in VCDcr are within 40% (mostly < 10%), and a greater change in surface reflectance tends to result in a larger change in VCDcr. In any given AOD bin, the magnitude of correlation between changes in surface reflectance and changes in VCDcr exceeds 0.8 (embedded red line). For a given bin of surface reflectance, by comparison, there is no apparent dependence of VCDcl changes on the amounts of AOD. The effects of surface reflectance on NO_2 VCDs are similar to the effects on VCDcr (Fig. 8b) due to the low CRF values on average (Fig. 7c, second column).

Figure 8d shows complex effects of surface reflectance perturbations on VCDcl. This is because the CP does not always change in the same direction as surface reflectance (see discussions above). When the OMI albedo is within ±0.05 of the MODIS BRF, the VCDcl tends to increase from case REF to SRF. There is greater scatter in VCDcl changes when the changes in surface reflectance are greater. In addition, VCDcl undergoes a much greater change in magnitude than VCDcr, reflecting the strong sensitivity of AMFcl to the CP.

3.3 Influences of implicit aerosol treatment on NO_2 and cloud retrievals

Case AER tests the effects of aerosols on NO_2 and cloud retrievals by setting AOD to zero during the retrieval process, thus mimicking the traditional treatment (Boersma et al., 2011; Bucsela et al., 2013). This procedure leads to changes in CF and CP that implicitly affect the subsequent NO_2 retrieval. If this implicit treatment results in the same NO_2 VCDs as case REF, then an explicit treatment of aerosols is no longer strictly desirable, as it is more expensive computationally.

Figures 7a and 7c show that at an annual scale, the exclusion of aerosols results in significant enhancements in CF and CRF. This is because aerosols reflect solar radiation to space, and exclusion of aerosols is compensated by an increase in effective CF and CRF (see Fig. 6) (Boersma et al., 2011; Lin et al., 2014b; Castellanos et al., 2015). Over China, the CF is enhanced from 0.04–0.15 in case REF to

0.06–0.30 in case AER. The increase is greatest over parts of east China with large AOD values in case REF. The CRF in case AER is greater than 0.35 over most of east China, compared to the values of 0.15–0.30 in case REF. Over the Sichuan Basin, the annual mean CRF exceeds 0.50 in case AER, more than doubling the CRF value (about 0.25) in case REF. Overall, the correlation between the amounts of AOD neglected in case AER and the level of CF (CRF) augmentation reaches a high value of 0.75 (0.82). Analyses of individual seasons also show large enhancements in CF and CRF as a result of neglecting aerosols (Figs. S2 and S4, third rows). Correlation between effective CF and AOT has been found for the eastern United States (0.66) (Boersma et al., 2011) and South America (Castellanos et al., 2015).

Figure 7b shows that excluding aerosols leads to an increase in CP from case REF to AER, in order to compensate for an otherwise reduction in the O_2-O_2 AMF. Over east China, the CP is increased from 700–900 hPa in case REF to 750–950 hPa in case AER. The CP enhancement is smaller over west China, and is smallest (0–20 hPa) over the Tibetan Plateau due to lowest aerosol loadings. However, the correlation between the amounts of AOD neglected in case AER and the amounts of CP increase is only 0.19, reflecting the complex effect aerosols on the CP retrieval (Lin et al., 2014b). The CP enhancements are apparent in all seasons (Fig. S3, third row).

Figure 5 (third row) shows the horizontal distribution of percentage NO_2 changes from case REF to AER. In all seasons, case AER is larger than REF by 0–40% over most of China. The overestimate is most obvious in central and south China, especially in winter (by 15–40%). By comparison, case AER leads to lower NO_2 VCDs by 0–20% over parts of the NCP in spring, many places in the north in winter, and parts of the west in non-summer seasons. At an annual scale, case AER leads to larger NO_2 VCDs than case REF by 0–40% over most regions. The magnitude of NO_2 changes are weakly correlated with the AOD or SSA (comparing Fig. 5, third row with Fig. 3). The degree of divergence in NO_2 changes is consistent with that found in Lin et al. (2014b).

The red solid lines in Fig. 9 present the AER to REF ratio for NO_2 VCDs on a monthly basis. Several representative regions of China are considered, including east China, west China, northern east China, Sichuan Basin, Beijing-Tianjin-Hebei (BTH), Yangtze River Delta (YRD), Pearl River Delta (PRD), and urban areas of Beijing, Shanghai and Guangzhou. These regions are defined in Fig. 1a. Figure 9 shows that for NO_2 VCDs averaged over a large region such as east or west China, the AER to REF ratio is close to 1 (0.9–1.1) in all months. For smaller regions, the deviation in the AER/REF ratio increases dramatically. The ratios vary between 0.8 and 1.4 across the 12 months for BTH, YRD and PRD, and between 0.8 and 1.6 for the urban areas of Beijing, Shanghai and Guangzhou. Whether case AER leads to larger or smaller NO_2 VCDs than case REF depends strongly on location and season. For urban Beijing, the maximum AER/REF ratio over the 12-month period is about twice as much as the minimum AER/REF ratio. Case AER has larger NO_2 VCDs than case REF in most months over the Sichuan Basin and the PRD, while the AER/REF ratios are more

seasonally variable in other regions. These regional and seasonal features call for comprehensive independent measurements to validate satellite retrievals.

Figure 10b shows the percentage changes in NO_2 VCDs from case REF to AER as a function of AOD and SSA. Here the percentage changes from all grid cells and months with respect to each bin of AOD (bin size = 0.05) and SSA (bin size = 0.01) are averaged; the amount of data in each bin is shown in Fig. 10a. Whether a larger AOD value corresponds to a greater enhancement in NO_2 VCD from case REF to AER depends in a complex manner on the SSA. This effect is also found by Castellanos et al. (2015) for biomass burning aerosols over South America. The largest increase (by 40–80%) from case REF to AER occurs with high AOD of 1–2 and low SSA of ~ 0.90. The dependence of NO_2 changes on SSA is weak, with positive correlations when AOD is below 1.5 and negative correlations when AOD exceeds 1.5.

Figures 10c presents the percentage changes in NO_2 VCDcr as a function of AOD and SSA. With a fixed AOD value, lower SSA tends to result in a smaller increase or a large decrease in VCDcr from case REF to AER; for AOD of 0.2–1.3, the correlation between VCDcr changes and SSA values exceeds 0.7. This is because stronger absorption diminishes the radiation that could otherwise be absorbed by NO_2, and leads to a consequent reduction in AMFcr. The dependence of VCDcr changes on AOD is highly SSA-sensitive. In many situations, the correlation between NO_2 changes and AOD or SSA values is weak (within ±0.5), owing to the indirect effects of aerosol vertical profiles and other factors. These features reflect the complex effects of aerosol extinction on the radiation absorbed by NO_2 under cloud-free conditions, as has been found in GEOS-Chem simulations (Lin et al., 2012). This contrasts to the effect of changing surface reflectance on NO_2 VCDcr such that an increase in surface reflectance reduces the amount of VCDcr (Fig. 8c).

Figure 10d shows that the effect of excluding aerosols on VCDcl differs significantly from the effect on VCDcr. Case AER leads to lower VCDcl values by 0–60% for a wide range of AOD and SSA, mostly because the increase in CP leads to a consequent enhancement of AMFcl.

We further elucidate how the exclusion of aerosols affects retrieved NO_2 VCDs. Changes in NO_2 VCD are determined by CRF, VCDcr and VCDcl (Eq. 2). Excluding aerosols leads to a general increase in CRF (and thus the weight of VCDcl) that is compensated by a decrease in VCDcl (due to an increase in CP). The change in VCDcr is more complex in sign, and to a lesser extent in magnitude. In most situations, the magnitude of VCDcr is much smaller than VCDcl (Fig. S5); this is because clouds are normally above the NO_2-concentrated layer, producing a "screening" effect on the radiation absorbed by NO_2. These factors explain the distinctive patterns of changes in NO_2 VCDcr, VCDcl and VCD from case REF to AER. For example, for AOD ~ 1.5 and SSA ~ 0.90, both VCDcr and VCDcl are reduced from case REF to AER, while the VCD is enhanced because CRF is much

enhanced and VCDcl greatly exceeds VCDcr.

In summary, inclusion or exclusion of aerosols has distinctive effects on three independent factors, CRF (or CF), VCDcr, and VCDcl (or CP). Section 3.5 will show the effect of excluding aerosols on the choice of "valid" data based on the CRF criterion. It follows that an implicit treatment of aerosols cannot fully account for the complex influences of aerosols on retrieved NO_2 VCDs.

3.4 Coupled effects of aerosols and surface reflectance on NO_2 retrieval

This section evaluates the coupled effects of perturbing aerosols and surface reflectance on retrieved NO_2 VCDs. For this purpose, we use Case S_A, which simultaneously adopts the OMI albedo from DOMINO v2 (following case SRF) and excludes aerosol information (following case AER) in the retrieval process. For this case, cloud parameters are also re-derived.

Figure 5 (fourth row) shows that, at an annual scale, case S_A leads to higher NO_2 VCDs than case REF over central east China, southwest China, Tibet and Qinghai. NO_2 VCDs are reduced by about 10% over parts of the NCP. Seasonal dependence is large for the NO_2 changes. Reductions over the NCP are most significant in spring (by 10–40%) followed by winter and fall. In summer, case S_A leads to general NO_2 enhancements by 0–40% over most of China, including the NCP. Over the Sichuan Basin, NO_2 VCDs in fall are increased by 20–40% from case REF to S_A, while the signs of change are more location-dependent in winter.

Figure 5 (fourth and fifth rows) shows that although case S_A follows the DOMINO v2 assumptions regarding surface reflectance and aerosols, in general it does not explain the differences between case REF and DOM. Therefore other factors are also important in differing case REF from DOM. They include NO_2 vertical profiles, cloud parameters, the pixel-specific radiative transfer calculation, and air pressure (Lin et al., 2014b).

Figure 11 further shows that the effect of changing surface reflectance on retrieved NO_2 VCDs interacts with the effect of excluding aerosol information. The figure presents the difference between (SRF – REF) + (AER – REF) and (S_A – REF) as a percentage fraction of REF. Positive values occur over most of China, i.e., the effect of simultaneously changing surface reflectance and aerosols is smaller than the summed effect of changing the two parameters individually. The magnitude of differences greatly depends on seasons and locations, and is largest in winter (by 5–20% over much of east China) and smallest in summer. These differences reflect the nonlinear influences of individual factors in retrieving NO_2, such that the effect of a particular parameter depends on other parameters (Lin et al., 2014b).

3.5 Discussion on the sampling of "valid" pixels and implications for analysis of pollution severity

Figure 12a shows the number of days per month with "valid" pixels based on the current criteria for cloud cover, snow/ice cover, and row-anomaly contamination. Averaged over China, fewer than half of the calendar days are included for analysis. For most of north China, about 12–20 days per month of 2012 are selected. The number of available days per month is below 8 over much of the south due to higher cloud coverage.

Changes in aerosols and surface reflectance both have a consequence on CF and CRF. The changes in CF and CRF in turn affect the number of retrieved NO_2 results that are determined "valid" under the usual criterion of CRF < 50%. With an implicit aerosol treatment (AER, S_A, and DOM), the CRF < 50% criterion designates pixels as invalid when more than half of the TOA radiance is from the combination of clouds and aerosols. With an explicit aerosol treatment (REF and SRF), however, the CRF < 50% criterion means that pixels are excluded if the clouds' contribution to the TOA radiance exceeds 50%. Thus the soundness of this criterion depends on how well the aerosol optical effects are quantified in the retrieval process, a critical factor in our explicit and physically more realistic aerosol treatment.

Case SRF has similar data coverage as case REF (Fig. 12b). Compared to case REF, case AER discards additional 2–10 days per month (or 15–60%) over most of east China because the aerosol-affected CRF exceeds 50% (Fig. 12c). This is consistent with the loss of 25% found by Lin et al. (2014b). Cases S_A and DOM also have much smaller numbers of valid days than does case REF (Figs. 12d and 12e).

For analyses of all retrievals in Sects. 3.1–3.4, we have evaluated retrieval results from the same set of pixels determined by case REF. In practice, however, information is not available on the pixels that could have been included in certain retrieval approaches but are instead discarded in other approaches. In such situations, a question is raised whether selecting different sets of satellite pixels will affect the evaluation of pollution severity and its subsequent applications. Of particular interest here is the loss of valid data by not explicitly accounting for aerosol optical effects (case AER versus REF).

Figure 9 contrasts NO_2 VCDs in case AER derived from pixels "valid" in case REF (solid red lines) versus from pixels "valid" in case AER (dashed red lines). Average VCDs for various representative regions of China are shown. A detailed horizontal distribution of their differences can be inferred by contrasting Fig. 5 (third row) and Fig. S6 (third row). Figure 9 shows a significant reduction in retrieved NO_2 VCDs by using the reduced set of "valid" data from case AER relative to the set determined by case REF. The reduction is about 10% averaged over east China, but exceeds 50% in some regions and months. Similar results are found for case DOM that also treats aerosol optical effects implicitly (Fig. 9, solid green versus dashed green lines). These results arise because high aerosol loadings are often coincident with high NO_2 pollution, due to similar emission sources and meteorological influences. Discarding pixels with high aerosols (that lead to significant increases in CRF from case REF to

AER and DOM) tends to exclude high NO_2 pollution situations as well (Lin et al., 2014b). This sampling bias is critical for determining the severity of NO_2 pollution from satellite remote sensing.

Explicit inclusion of aerosols in the retrieval process (as in case REF or POMINO) will avoid the sampling bias caused by removal of strong-pollution situations, especially if aerosol information can be adequately constrained. In publishing the POMINO data, we elect to include pixels with high aerosol loadings, although we note that these pixels may contain larger uncertainties for NO_2 than those with low aerosol content, since we do not have fully accurate aerosol information. This choice is supported in part by our previous comparisons against MAX-DOAS NO_2 data (Lin et al., 2014b) and by the fact that the AOD values are relatively well constrained by MODIS on a monthly basis. We publish the AOD and SSA values together with NO_2 VCDs, so that users can choose whether or not to include high-aerosol situations.

4. Impacts of aerosols and surface reflectance on OMI-based NO_x emission constraint

Sections 3.2–3.5 show the sensitivity of retrieved NO_2 VCDs to various treatments of aerosols and surface reflectance. This section further analyzes the influences on subsequent NO_x emission constraint, a popular application of OMI data. NO_2 VCDs retrieved via different approaches are used to optimize NO_x emissions. We focus on anthropogenic emissions in China. As discussed in Sect. 3.5, the set of "valid" OMI pixels depends on the retrieval approach. Thus this section also identifies the effects of selecting various sets of "valid" pixels.

Top-down emissions are derived for individual months in 2012 on a 0.25 ° long. x 0.25 ° lat. grid, by scaling the *a priori* emissions (assumed in GEOS-Chem) with the ratio of OMI-derived to CTM-modeled NO_2 VCDs (Martin et al., 2003). Model NO_2 values (at 0.667 ° long. x 0.5 ° lat.) are sampled at times and locations coincident with valid OMI pixels, and are then re-mapped to the 0.25 ° long. x 0.25 ° lat. grid; see Fig. S7 for the horizontal distribution of model NO_2. The scaling approach here assumes local mass balance (Leue et al., 2001). It does not fully account for the horizontal transport of NO_x nor the dependence of NO_x lifetime on emissions (Turner et al., 2012); these two factors are likely to result in a small difference (within 10%) in top-down total Chinese emissions (Lin, 2012). Also, the same scaling is applied to both anthropogenic and natural emissions. Lin (2012) presents an approach that takes advantage of the distinctive seasonality in various emission sources to better distinguish anthropogenic from natural sources. They found similar changes (from *a priori* to top-down) in anthropogenic and natural emissions when summed over China.

The *a posteriori* emissions are calculated as a weighted average of *a priori* and top-down emissions, by assuming normal distributions of errors in these emissions. Following Lin (2012), errors in anthropogenic emissions are taken as 60% for *a priori*

and 52% for top-down (for combined errors in model simulations [40%, Lin et al., 2012; Yan et al., 2014], satellite NO_2 retrievals [~30%, Boersma et al., 2011; Lin et al., 2014b], and emission inversion procedures [12%, Lin, 2012]). The same errors are assigned to all grid cells, following Lin (2012). This leads to an error of 39% in the *a posteriori* emissions. Although the actual errors may be larger for individual locations, there is no such detailed information for emission constraint.

Figure 13b shows the horizontal distribution of annual mean *a posteriori* emissions in 2012 derived from case REF. The spatial pattern is close to that of the *a priori* emissions (Fig. 13a) with largest values located at cities. The *a posteriori* emissions are lower than *a priori* values by 0–40% over most of east China, with enhancements at many high-emission hotspots and over the southern coastal provinces (Fig. 13c).

Table 3 shows that for China as a whole, the *a posteriori* emissions in case REF are 9.05 TgN yr^{-1}, about 9.3% smaller than the *a priori* emissions at 9.78 TgN yr^{-1}. For east China (101.25°E–126.25°E, 20°N–46°N), the REF *a posteriori* emissions for 2012 total at 8.43 TgN yr^{-1}, about 19% higher than the estimate for 2006 by Lin (2012). This increase likely reflects the recent growth of NO_x pollution in China after its recovery from the economic downturn (Lin and McElroy, 2011).

Figures 13h–13k present the percentage differences in *a posteriori* emissions comparing results from case REF to those from the other retrieval cases. OMI pixels are selected when they are deemed to be "valid" according to criteria specific to individual retrieval cases; here each retrieval case has a distinctive set of "valid" pixels. Locations with emissions lower than 0.5 x 10^{15} cm^{-2} hr^{-1} (totaling at 11% of Chinese emissions) are masked to highlight the polluted areas. Overall, the magnitude of emission changes is highly region-dependent. Across China with few exceptions, case SRF produces emissions similar to REF. Differences are much larger between case REF and AER. Compared to case REF, case AER produces lower emissions by 5–10% over the NCP but higher emissions by 5–30% over many other regions; the greatest enhancements occur over the Sichuan Basin and PRD. Compared to REF and AER, case S_A results in smaller emissions over the NCP. Case S_A produces emissions slightly larger than case REF in the Sichuan Basin, PRD, and many other southern provinces. By comparison, case DOM (exactly the same as DOMINO v2) leads to larger *a posteriori* emissions than does case REF, by 0–40% over most of China. Table 3 shows that total Chinese emissions in all cases are within 3% of values from case REF; this closeness is due mainly to compensation between region-dependent positive and negative differences.

Figures 13d–13g show the percentage differences in *a posteriori* emissions comparing case REF to other retrieval cases, but now based on a single set of "valid" pixels determined by case REF. Locations with emissions lower than 0.5 x 10^{15} cm^{-2} hr^{-1} are masked to highlight the polluted areas. Case SRF leads to similar emissions as case REF. Case AER exceeds REF by 0–30% over most regions, but with reductions by 0–5% over parts of north China. Case S_A is also larger than REF over much of

China. Case DOM exceeds REF by 0–40% especially over the Sichuan Basin and parts of north China.

Differences between Figs. 13e–13g and Figs. 13i–13k are apparent – a result of different pixel sampling. The differences over the NCP indicate that, since the implicit treatment of aerosols in cases AER, S_A and DOM leads to exclusion of situations with high aerosol loadings (and coincidently high NO_2 pollution; see Sect. 3.5), there is a consequent underestimate in the *a posteriori* emissions.

Figures 14a, 14d and 14g show the contrasts between case REF and AER for the ratio of maximum to minimum monthly *a posteriori* emissions. Locations are shown only with emissions greater than 0.5×10^{15} cm^{-2} hr^{-1}. For case REF (Fig. 14a), the max/min ratios range from 1 to 10, but are about 2–5 at most locations. Figure 14d (based on REF-determined valid pixels) shows enhancements in the max/min ratio from case REF to AER over most of China. By comparison, Fig. 14g (based on case-specific sets of valid pixels) shows that case AER leads to much larger max/min ratios over most of south China, while the changes in max/min ratios are more location-dependent over the NCP. Figure 14 further contrasts case REF and AER for the months of maximum and minimum emissions. For case REF, minimum emissions often occur in May–September in the NCP, in contrast to December–March in many southern areas (Fig. 14b). Maximum emissions occur in November–February over most of China (Fig. 14c). Case AER leads to location-dependent shifts in the months of maximum and minimum emissions (Figs. 14e, 14f, 14h, and 14i); further, these shifts are more apparent when OMI pixels are selected with respect to individual retrieval approaches (Figs., 14h and 14i). These differences highlight the seasonal and spatial dependence of constrained emissions on the NO_2 retrieval approaches.

5. Conclusion

This paper presents an improved retrieval, the POMINO algorithm, of tropospheric NO_2 VCDs over China in 2012, by explicitly accounting for temporally and spatially varying aerosol optical effects and surface reflectance anisotropy. Prerequisite cloud optical parameters (CF and CP) are retrieved with the same treatments for aerosols and surface, thus eliminating any algorithm inconsistency in retrieving NO_2 and clouds. Our NO_2 retrieval is focused on calculations of tropospheric AMFs, taking the tropospheric SCDs from DOMINO v2. Our cloud retrieval starts from the SCDs of O_2-O_2 in OMCLDO2 v3. Aerosol vertical profiles and optical properties are first taken from GEOS-Chem simulations, with subsequent AOD constraints based on monthly MODIS/Aqua data. Surface reflectance data over lands are taken from the MODIS BRDF product. Retrievals are performed for individual OMI pixels via on-line radiative transfer calculations without the need for look-up tables, thanks to the newly parallelized AMFv6 code driven by LIDORT v3.6. Sensitivity tests are performed to evaluate the effect of an explicit (as opposed to an implicit) treatment of aerosols and the effect of changes in surface reflectance characteristics on retrieved NO_2 VCDs. Additional analyses are done for subsequent OMI-based NO_x emission

constraints. Results are presented as monthly mean values on a 0.25 °long. x 0.25 °lat. grid.

POMINO NO_2 VCDs undergo strong seasonal and spatial variability. Large NO_2 VCDs are located in east China due to significant anthropogenic emissions. On an annual basis, NO_2 VCDs vary from 15–25 x 10^{15} cm^{-2} over the NCP to below 10^{15} cm^{-2} over much of west China. Over the polluted regions, NO_2 VCDs reach maxima in winter and minima in summer, due mostly to the seasonal variation in NO_x lifetime. Over cleaner regions (e.g., much of west China), NO_2 VCDs peak in summer with minima in winter, because strong natural emissions in summer overcompensate for the short NO_2 lifetime. The maximum to minimum ratio in monthly mean NO_2 VCDs is about 3.6 for regions east of 101.25 °E as a whole and about 1.4 over the west. A POMINO-based NO_x emission constraint leads to *a posteriori* Chinese anthropogenic emissions at 9.05 TgN yr^{-1}, an increase from 2006 (Lin, 2012) by about 19%.

In one sensitivity test, we re-retrieved clouds and NO_2 VCDs, by adopting the monthly climatological OMI albedo data (OMLER v1) in place of the MODIS BRDF data. Surface reflectance is greatly enhanced over most of east China and reduced over the west. Changes in surface reflectance result in changes of opposite sign in CF with more complex effects on CP. As a consequence, annual mean NO_2 VCDs are decreased by 5–15% over central and south China with enhancements over many other regions. The reductions in south China are largest (15–40%) in fall, but are replaced by slight enhancements in summer. On an annual basis, changes in surface reflectance have a small effect (within 5%) on constrained NO_x emissions over most Chinese locations with anthropogenic emissions greater than 0.5 x 10^{15} cm^{-2} hr^{-1}.

In another sensitivity test, an implicit treatment of aerosols mimics the traditional algorithms by excluding aerosol information in retrieving clouds and NO_2 VCDs. The implicit treatment greatly enhances effective CF (spatial correlation = 0.75 between neglected annual mean AOD values and CF enhancements), CRF (correlation = 0.82), and CP (correlation = 0.19). The low correlation for CP highlights the complexity of aerosol effects. Changes in NO_2 VCDs from an explicit to an implicit treatment of aerosols depend in a complex manner on AOD, SSA, heights of aerosols relative to NO_2, and other factors; these factors affect CRF, VCDcl and VCDcr that determine NO_2 VCDs. The annual mean NO_2 VCDs are enhanced by 15–40% over much of east China. The seasonal and spatial variability of NO_2 changes is apparent. NO_2 VCDs are reduced by 10–20% over parts of the NCP in spring and over north China in winter, whereas these reductions are replaced by general enhancements in summer and fall. The effect on subsequently-constrained annual NO_x emissions varies between -5% and 30% over east China with apparent seasonal and regional dependence.

For the usual criterion of CRF < 50% to select "valid" pixels, the large enhancements in CRF due to an implicit aerosol treatment result in significant reductions in the number of days with "valid" pixels over polluted regions (by 2–10 days per month, or 15–60%, on average). This also leads to a likely sampling bias due to the exclusion of

high-aerosol days that often experience high NO_2 pollution, consistent with the findings of Lin et al. (2014b).

The effect of an implicit aerosol treatment on retrieved NO_2 VCDs also interacts with the effect of changes in surface reflectance. NO_2 changes obtained by simultaneously excluding aerosol information and adopting the OMI albedo are smaller than the overall NO_2 changes obtained by making these two adjustments individually and summing the results. Although these adjustments (no aerosols + OMI albedo) are present in the DOMINO v2 approach, the resulting NO_2 VCDs still differ from those of DOMINO v2, indicating the importance of differences between other factors assumed in the retrieval processes (e.g. NO_2 profile shape, atmospheric profile in O_2-O_2 retrieval, pixel-by-pixel radiative transfer calculation versus look-up table, and air pressure).

There are no sufficiently comprehensive independent measurements available to systematically evaluate the various NO_2 retrieval approaches. Current MAX-DOAS measurements are very limited over China, with few sites and short operation periods (Irie et al., 2012; Ma et al., 2013; Hendrick et al., 2014; Kanaya et al., 2014). In situ measurements are rare for vertical profiles of aerosols and NO_2. Our results show that the effects of aerosols and surface reflectance are highly season- and location-dependent. This clearly indicates the need for a comprehensive measurement network to validate satellite data. Nonetheless, our present study and that of Lin et al. (2014b) point the way forward for a physically more realistic NO2 retrieval by explicit inclusion of aerosol effects.

Currently, our POMINO NO_2 data are available for 2004–2013 (http://www.atmos.pku.edu.cn/acm/acmModel.html#POMINO). Daily level-3 data on a 0.25° long. x 0.25° lat. grid are provided on the webpage for general users, and level-2 data (including averaging kernels) can be provided for advanced users upon request. We simultaneously provide daily AOD, SSA and surface reflectance (MODIS BRF over lands and OMLER v3 albedo over the oceans) data for users. We elect to include daily NO_2 data with high aerosol loadings to reduce the potential sampling bias, in line with our choice of an explicit aerosol treatment and as supported by Lin et al. (2014b). We note that these NO_2 data with high aerosol pollution may be subject to larger uncertainties, since aerosols are not fully accurately constrained by observations. Users can make their own judgment on whether to include the NO_2 data with high aerosol pollution. With more aerosol data from satellite, ground and in situ measurements in the future, aerosol optical effects can be better constrained to reduce the associated uncertainties in NO_2 retrievals.

Our parallelized LIDORT-driven AMFv6 code is also available for public use. With 16 computational cores (Intel (R) Xeon (R) CPU X7550 @ 2.00GH) running in parallel, it takes about 3 hours of wall-clock time to retrieve both cloud parameters and NO_2 VCDs over China for a month; the retrieval process includes pixel-specific radiative transfer calculations and explicit treatments of aerosols and surface

reflectance anisotropy. The excellent scalability of our parallelized code means that additional computational cores can be employed to further speed up the retrieval process. Such retrieval efficiency enables a fast global retrieval that will be particularly important for future fine-resolution satellite instruments such as TropOMI (which is expected to have a data rate ~8 times that of OMI) and GEMS (which will be onboard a geostationary satellite with hourly measurements at a horizontal resolution of 5 x 15 km^2).

Acknowledgments

This research is supported by the National Natural Science Foundation of China, grants 41175127 and 41422502, and by the 973 program, grant 2014CB441302. We acknowledge the free use of NO_2 and cloud products from www.temis.nl, GMTED2010 surface elevation data from USGS, GLCNMO land use type data from ISCGM, MODIS aerosol and surface reflectance data from NASA, and several AOD measurements from AERONET. Folkert Boersma acknowledges receiving funding for this research from NWO Vidi Grant 864.09.001 and from the European Community's Seventh Framework Programme under grant agreement n ° 607405 (QA4ECV). The calculation was supported in part by the National Institute of Supercomputing and Network/Korea Institute of Science and Technology Information with supercomputing resources including technical support (KSC-2014-C2-034).

Appendix A. GEOS-Chem simulations

We adopted vertical profiles of NO_2 and aerosol optical parameters from GEOS-Chem simulations on a 0.667 ° long. x 0.5 ° lat. grid. We used the latest version 9-02, which is an update of version v8-03-02 employed by Lin et al. (2014b). Here we summarize the model updates relevant to our retrieval study. The reader is referred to Lin et al. (2014b) for a general model description.

GEOS-Chem simulates spatiotemporally varying concentrations of NO_x and other gaseous and aerosol species. It also outputs optical properties of various aerosol types, including secondary inorganic aerosols (sulfates, nitrates, and ammoniums), organic aerosols, black carbon, dust and sea salts. Vertical profiles and type-specific optical properties of aerosols are available for our NO_2 retrieval, including size distributions, refractive indices, AOD, SSA, phase function, and hygroscopic growth rates (Drury et al., 2010). The simulations have been conducted from 2004 to 2013 to facilitate our NO_2 retrieval.

For Chinese anthropogenic emissions, we used the latest MEIC inventory for NO_x and other gaseous species with a base year of 2008 (www.meicmodel.org). The inventory is an update of the previous INTEX-B inventory. We followed Huang et al. (2012) for anthropogenic emissions of ammonia. Other emission setups are the same as those in Lin et al. (2014b). In China, anthropogenic emissions of NO_x have varied significantly in recent years. Thus we calculated the ratios of DOMINO v2 NO_2 VCDs in 2008 to other years on a 0.25 ° long. x 0.25 ° lat. grid, and then applied the

ratios to scale NO_x emissions to the respective years. Such scaling is tantamount to a first-order emission adjustment to reduce the effect of emission-dependent NO_x lifetime on emission constraints in Sect. 4.

We implemented seasonality for Chinese residential emissions to reflect its current residential heating scheme (Streets et al., 2003). Residential emissions are caused by stove operation. As a modification of the piecewise method by Streets et al. (2003), we assumed that residential stoves operate 16 hours per day (hr d^{-1}) for monthly mean 2-m air temperature below 0 ℃, 3 hr d^{-1} for temperature above 10 ℃, and 3–16 hr d^{-1} in between the two temperatures (linear interpolation). Monthly mean air temperature is taken from the GEOS-5 meteorological fields and averaged over 2005–2009. As such, residential emissions are largest in winter and smallest in summer. The seasonality is not important for NO_x since residential emissions contribute to 5.6% of total emissions only (Zhang et al., 2009). By comparison, seasonality has a large impact on black carbon, for which pollutant residential sources contribute 55% of total anthropogenic emissions in China (Zhang et al., 2009). The emission seasonality greatly affects the SSA of total aerosols.

GEOS-Chem employs a non-local scheme to simulate vertical mixing in the boundary layer (Lin and McElroy, 2010) and a modified Relaxed Arakawa-Schubert scheme for convection (Rienecker et al., 2008). GEOS-Chem captures vertical profiles of NO_2 and ozone over the United States from aircraft measurements (Lin and McElroy, 2010). The same schemes are used for NO_2 and aerosols – thus, errors in the height of aerosols relative to NO_2 may be smaller than errors in their absolute heights. This is important for reducing the sensitivity of retrieved NO_2 VCDs to errors in the vertical profiles of aerosols, given the lack of observational constraints on their profiles. Figure A1, as an illustration, presents vertical profiles of NO_2 volume mixing ratios (VMRs), aerosol extinction coefficients (AECs), SSA, AMFs, clear-sky AMFs, and cloudy-sky AMFs at the beginning of January, April, July and October at representative pixels in four regions: urban Beijing, south China, Tibet, and the oceans. Figure A1 shows that over the polluted east China, NO_2 and aerosols are often collocated in the boundary layer. Over Tibet and the oceans (clear air), there exist large amounts of NO_2 above the aerosol layer. A comparison of our NO_2 profiles with those in DOMINO v2 (based on the TM4 model) is presented in Fig. 3 of Lin et al. (2014b).

Appendix B. Using MODIS AOD to constrain GEOS-Chem AOD

We used MODIS/Aqua AOD data from the MYD04 Collection 5.1 level-2 dark-target product (Remer et al., 2008) to constrain model AOD on a monthly basis. Adjustments were done at a wavelength of 550 nm.

We first projected the level-2 MODIS AOD data to the GEOS-Chem 0.667 ° long. x 0.5 ° lat. grid for each day, in order to perform a subsequent calculation of monthly means. The derived monthly mean MODIS data are subject to missing values, due to

stringent cloud screening and difficulties in retrieving AOD above snow/ice-covered or bare/deserted lands. Thus, we conducted temporal and spatial interpolation upon the monthly mean data. We used the average of monthly mean values from previous and successive months to fill the missing value in a particular month (first the adjacent two months, then the adjacent four months, and so on); the missing value was filled when at least two adjacent months with valid data were found. For the temporal interpolation, we made use of monthly data from 2004 to 2013. For grid cells containing missing values after the temporal interpolation, we performed subsequent spatial interpolation in a similar manner: first the adjacent 5 x 5 = 25 grid cells were used, and then the adjacent 7 x 7 = 49 grid cells, and so on. A missing value was filled when at least 15 adjacent grid cells are deemed to be valid. Figure S8 presents the AOD values before and after this interpolation.

We note here that the latest MODIS Collection 6 product provides a dataset merging results from the "dark-target" and the "deep-blue" algorithms; this merger greatly reduces the number of missing values (Sayer et al., 2014). The dark-target algorithm has changed little from Collection 5.1 to 6. In the future, we plan to adopt this new dataset to minimize the need for data interpolation.

We used the data-filled monthly mean MODIS AOD data to adjust GEOS-Chem model results. To facilitate the adjustment, a corresponding monthly mean model dataset was made. We selected model AOD at times coincident with pre-data-filling MODIS data, and then went through the same temporal and spatial interpolation process to generate a corresponding data-filled monthly mean dataset.

For a given month, differences between the data-filled monthly mean MODIS and model AOD data sets were used to adjust the original model results for each day of the month. We deployed two adjustment methods. The primary method calculates the ratio of data-filled monthly mean MODIS AOD to data-filled model AOD and then applies this ratio to scale model results for all days of the respective month. This scaling method can lead to unrealistically large AOD for certain grid cells. In this eventuality, we simply calculated the arithmetic difference between data-filled monthly mean MODIS AOD and data-filled model AOD, and applied this difference to the original model AOD for all days of the month. This secondary adjustment was applied when the scaling factor exceeded a threshold of 3, or when the monthly mean (from all days) of the original model AOD multiplied by the scaling factor exceeded a value of 1.5.

To validate our model adjustment, we compared the post-adjustment model AOD with independent AOD data from the two ground measurement networks AERONET (Holben et al., 1998) and CSHNET (Xin et al., 2007). These two networks encompass a total of 19 sites across China, with various ground conditions and aerosol loadings; see Lin et al. (2014c) for detailed descriptions of these ground networks. The scatter plot in Fig. A2 compares the post-adjustment model data with ground networks in 2006. The post-adjustment model AOD are consistent with ground networks, with a

correlation of 0.74, a small mean bias of -0.02 (5%), a reduced major axis regression slope of 1.01 and an intercept of -0.03. We therefore conclude that the model adjustment leads to a reasonable AOD constraint.

References

Acarreta, J. R., De Haan, J. F., and Stammes, P.: Cloud pressure retrieval using the O-2-O-2 absorption band at 477 nm, Journal of Geophysical Research-Atmospheres, 109, D05204, doi:10.1029/2003jd003915, 2004.

Boersma, K. F., Eskes, H. J., and Brinksma, E. J.: Error analysis for tropospheric NO2 retrieval from space, J. Geophys. Res., 109, D04311, doi:10.1029/2003JD003962, 2004.

Boersma, K. F., Eskes, H. J., Dirksen, R. J., A, R. J. v. d., Veefkind, J. P., Stammes, P., Huijnen, V., Kleipool, Q. L., Sneep, M., Claas, J., Leitão, J., Richter, A., Zhou, Y., and Brunner, D.: An improved tropospheric NO2 column retrieval algorithm for the Ozone Monitoring Instrument, Atmos. Meas. Tech., 4, 1905-1928, doi:10.5194/amt-4-1905-2011, 2011.

Bucsela, E. J., Krotkov, N. A., Celarier, E. A., Lamsal, L. N., Swartz, W. H., Bhartia, P. K., Boersma, K. F., Veefkind, J. P., Gleason, J. F., and Pickering, K. E.: A new stratospheric and tropospheric NO2 retrieval algorithm for nadir-viewing satellite instruments: applications to OMI, Atmos. Meas. Tech. , 6, 2607-2626, doi:10.5194/amt-6-2607-2013, 2013.

Castellanos, P., and Boersma, K. F.: Reductions in nitrogen oxides over Europe driven by environmental policy and economic recession, Sci. Rep., 2, 265, doi:10.1038/srep00265, 2012.

Castellanos, P., Boersma, K. F., Torres, O., and de Haan, J. F.: OMI tropospheric NO2 air mass factors over South America: effects of biomass burning aerosols, Atmos. Meas. Tech. Discuss., 8, 2683-2733, doi:10.5194/amtd-8-2683-2015, 2015.

Che, H. Z., Yang, Z. F., Zhang, X. Y., Zhu, C. Z., Ma, Q. L., Zhou, H. G., and Wang, P.: Study on the aerosol optical properties and their relationship with aerosol chemical compositions over three regional background stations in China, Atmospheric Environment, 43, 1093-1099, doi:10.1016/j.atmosenv.2008.11.010, 2009.

Cooper, O. R., Parrish, D. D., Stohl, A., Trainer, M., Nedelec, P., Thouret, V., Cammas, J. P., Oltmans, S. J., Johnson, B. J., Tarasick, D., Leblanc, T., McDermid, I. S., Jaffe, D., Gao, R., Stith, J., Ryerson, T., Aikin, K., Campos, T., Weinheimer, A., and Avery, M. A.: Increasing springtime ozone mixing ratios in the free troposphere over western North America, Nature, 463, 344-348, doi:10.1038/nature08708, 2010.

Dirksen, R. J., Boersma, K. F., Eskes, H. J., Ionov, D. V., Bucsela, E. J., Levelt, P. F.,

and Kelder, H. M.: Evaluation of stratospheric NO2 retrieved from the Ozone Monitoring Instrument: Intercomparison, diurnal cycle, and trending, Journal of Geophysical Research-Atmospheres, 116, D08305, doi:10.1029/2010jd014943, 2011.

Drury, E., Jacob, D. J., Spurr, R. J. D., Wang, J., Shinozuka, Y., Anderson, B. E., Clarke, A. D., Dibb, J., McNaughton, C., and Weber, R.: Synthesis of satellite (MODIS), aircraft (ICARTT), and surface (IMPROVE, EPA-AQS, AERONET) aerosol observations over eastern North America to improve MODIS aerosol retrievals and constrain surface aerosol concentrations and sources, Journal of Geophysical Research-Atmospheres, 115, D14204, doi:10.1029/2009jd012629, 2010.

Ford, B., and Heald, C. L.: An A-train and model perspective on the vertical distribution of aerosols and CO in the Northern Hemisphere, Journal of Geophysical Research-Atmospheres, 117, D06211, doi:10.1029/2011jd016977, 2012.

Hendrick, F., Müller, J.-F., Clémer, K., Wang, P., Mazière, M. D., Fayt, C., Gielen, C., Hermans, C., Ma, J., and Pinardi, G.: Four years of ground-based MAX-DOAS observations of HONO and NO 2 in the Beijing area, Atmospheric Chemistry and Physics, 14, 765-781, 2014.

Holben, B. N., Eck, T. F., Slutsker, I., Tanre, D., Buis, J. P., Setzer, A., Vermote, E., Reagan, J. A., Kaufman, Y. J., Nakajima, T., Lavenu, F., Jankowiak, I., and Smirnov, A.: AERONET - A federated instrument network and data archive for aerosol characterization, Remote Sensing of Environment, 66, 1-16, 1998.

Huang, X., Song, Y., Li, M., Li, J., Huo, Q., Cai, X., Zhu, T., Hu, M., and Zhang, H.: A high - resolution ammonia emission inventory in China, Global Biogeochemical Cycles, 26, GB1030, doi:10.1029/2011GB004161, 2012.

Hyer, E. J., Reid, J. S., and Zhang, J.: An over-land aerosol optical depth data set for data assimilation by filtering, correction, and aggregation of MODIS Collection 5 optical depth retrievals, Atmospheric Measurement Techniques, 4, 379-408, doi:10.5194/amt-4-379-2011, 2011.

Irie, H., Boersma, K. F., Kanaya, Y., Takashima, H., Pan, X., and Wang, Z. F.: Quantitative bias estimates for tropospheric NO2 columns retrieved from SCIAMACHY, OMI, and GOME-2 using a common standard for East Asia, Atmospheric Measurement Techniques, 5, 2403-2411, doi:10.5194/amt-5-2403-2012, 2012.

Jiang, Z., Worden, J. R., Jones, D. B. A., Lin, J.-T., Verstraeten, W. W., and Henze, D. K.: Constraints on Asian ozone using Aura TES, OMI and Terra MOPITT, Atmos. Chem. Phys., 15, 99-112, doi:10.5194/acp-15-99-2015, 2015.

Kanaya, Y., Irie, H., Takashima, H., Iwabuchi, H., Akimoto, H., Sudo, K., Gu, M., Chong, J., Kim, Y., and Lee, H.: Long-term MAX-DOAS network observations of

NO2 in Russia and Asia (MADRAS) during the period 2007–2012: instrumentation, elucidation of climatology, and comparisons with OMI satellite observations and global model simulations, Atmospheric Chemistry and Physics, 14, 7909-7927, 2014.

Kleipool, Q. L., Dobber, M. R., de Haan, J. F., and Levelt, P. F.: Earth surface reflectance climatology from 3 years of OMI data, Journal of Geophysical Research-Atmospheres, 113, D18308, doi:10.1029/2008jd010290, 2008.

Lamsal, L. N., Martin, R. V., Padmanabhan, A., van Donkelaar, A., Zhang, Q., Sioris, C. E., Chance, K., Kurosu, T. P., and Newchurch, M. J.: Application of satellite observations for timely updates to global anthropogenic NO(x) emission inventories, Geophysical Research Letters, 38, L05810, doi:10.1029/2010gl046476, 2011.

Lee, K. H., Li, Z., Wong, M. S., Xin, J., Wang, Y., Hao, W. M., and Zhao, F.: Aerosol single scattering albedo estimated across China from a combination of ground and satellite measurements, J. Geophys. Res., 112, D22S15, doi:10.1029/2007JD009077, 2007.

Leue, C., Wenig, M., Wagner, T., Klimm, O., Platt, U., and Jähne, B.: Quantitative analysis of NOx emissions from Global Ozone Monitoring Experiment satellite image sequences, J. Geophys. Res., 106(D6), 5493–5505, doi:10.1029/2000JD900572, 2001.

Levelt, P. F., van den Oord, G. H., Dobber, M. R., Malkki, A., Visser, H., de Vries, J., Stammes, P., Lundell, J. O., and Saari, H.: The ozone monitoring instrument, Geoscience and Remote Sensing, IEEE Transactions on, 44, 1093-1101, 2006.

Lin, J.-T., and McElroy, M. B.: Detection from space of a reduction in anthropogenic emissions of nitrogen oxides during the Chinese economic downturn, Atmospheric Chemistry and Physics, 11, 8171-8188, doi:10.5194/acp-11-8171-2011, 2011.

Lin, J.-T., Liang, X.-Z., and Wuebbles, D. J.: Effects of Intercontinental Transport on Surface Ozone over the United States: Present and Future Assessment with a Global Model, Geophys. Res. Lett., 35, doi:10.1029/2007GL031415, 2008.

Lin, J.-T., Nielsen, C. P., Zhao, Y., Lei, Y., Liu, Y., and McElroy, M. B.: Recent Changes in Particulate Air Pollution over China Observed from Space and the Ground: Effectiveness of Emission Control, Environmental Science & Technology, 44, 7771-7776, doi:10.1021/es101094t, 2010a.

Lin, J.-T., Pan, D., Davis, S. J., Zhang, Q., He, K., Wang, C., Streets, D. G., Wuebbles, D. J., and Guan, D.: China's international trade and air pollution in the United States, Proceedings of the National Academy of Sciences, doi:10.1073/pnas.1312860111, 2014a.

Lin, J.-T., Martin, R. V., Boersma, K. F., Sneep, M., Stammes, P., Spurr, R., Wang, P., Van Roozendael, M., Clémer, K., and Irie, H.: Retrieving tropospheric nitrogen

dioxide from the Ozone Monitoring Instrument: effects of aerosols, surface reflectance anisotropy, and vertical profile of nitrogen dioxide, Atmos. Chem. Phys., 14, 1441-1461, doi:10.5194/acp-14-1441-2014, 2014b.

Lin, J.: Satellite constraint for emissions of nitrogen oxides from anthropogenic, lightning and soil sources over East China on a high-resolution grid, Atmos. Chem. Phys., 12, 2881-2898, doi:10.5194/acp-12-2881-2012, 2012.

Lin, J., van Donkelaar, A., Xin, J., Che, H., and Wang, Y.: Clear-sky aerosol optical depth over East China estimated from visibility measurements and chemical transport modeling, Atmospheric Environment, 95, 257-267, doi:10.1016/j.atmosenv.2014.06.044, 2014c.

Lin, J. T., and McElroy, M. B.: Impacts of boundary layer mixing on pollutant vertical profiles in the lower troposphere: Implications to satellite remote sensing, Atmospheric Environment, 44, 1726-1739, doi:10.1016/j.atmosenv.2010.02.009, 2010.

Lin, J. T., McElroy, M. B., and Boersma, K. F.: Constraint of anthropogenic NOx emissions in China from different sectors: a new methodology using multiple satellite retrievals, Atmospheric Chemistry and Physics, 10, 63-78, 2010b.

Lin, J. T., Liu, Z., Zhang, Q., Liu, H., Mao, J., and Zhuang, G.: Modeling uncertainties for tropospheric nitrogen dioxide columns affecting satellite-based inverse modeling of nitrogen oxides emissions, Atmospheric Chemistry and Physics, 12, 12255-12275, doi:10.5194/acp-12-12255-2012, 2012.

Liu, J., Kuang, W., Zhang, Z., Xu, X., Qin, Y., Ning, J., Zhou, W., Zhang, S., Li, R., and Yan, C.: Spatiotemporal characteristics, patterns, and causes of land-use changes in China since the late 1980s, Journal of Geographical Sciences, 24, 195-210, 2014.

Lucht, W., Schaaf, C. B., and Strahler, A. H.: An algorithm for the retrieval of albedo from space using semiempirical BRDF models, Ieee Transactions on Geoscience and Remote Sensing, 38, 977-998, doi:10.1109/36.841980, 2000.

Ma, J. Z., Beirle, S., Jin, J. L., Shaiganfar, R., Yan, P., and Wagner, T.: Tropospheric NO2 vertical column densities over Beijing: results of the first three years of ground-based MAX-DOAS measurements (2008-2011) and satellite validation, Atmospheric Chemistry and Physics, 13, 1547-1567, doi:10.5194/acp-13-1547-2013, 2013.

Maasakkers, J. D.: Vital improvements to the retrieval of tropospheric NO2 columns from the Ozone Monitoring Instrument, Eindhoven University of Technology, Eindhoven, 2013.

Martin, R. V., Jacob, D. J., Chance, K., Kurosu, T. P., Palmer, P. I., and Evans, M. J.:

Global inventory of nitrogen oxide emissions constrained by space-based observations of NO2 columns, J. Geophys. Res., 108, 4537, doi:10.1029/2003JD003453, 2003.

Mijling, B., van der A, R., and Zhang, Q.: Regional nitrogen oxides emission trends in East Asia observed from space, Atmospheric Chemistry and Physics, 13, 12003-12012, 2013.

Miyazaki, K., and Eskes, H.: Constraints on surface NOx emissions by assimilating satellite observations of multiple species, Geophysical Research Letters, 40, 4745-4750, 2013.

Noguchi, K., Richter, A., Rozanov, V., Rozanov, A., Burrows, J. P., Irie, H., and Kita, K.: Effect of surface BRDF of various land cover types on geostationary observations of tropospheric NO2, Atmospheric Measurement Techniques, 7, 3497-3508, doi:10.5194/amt-7-3497-2014, 2014.

Palmer, P. I., Jacob, D. J., Chance, K., Martin, R. V., Spurr, R. J. D., Kurosu, T. P., Bey, I., Yantosca, R., Fiore, A., and Li, Q. B.: Air mass factor formulation for spectroscopic measurements from satellites: Application to formaldehyde retrievals from the Global Ozone Monitoring Experiment, Journal of Geophysical Research-Atmospheres, 106, 14539-14550, doi:10.1029/2000jd900772, 2001.

Remer, L. A., Kleidman, R. G., Levy, R. C., Kaufman, Y. J., Tanre, D., Mattoo, S., Martins, J. V., Ichoku, C., Koren, I., Yu, H. B., and Holben, B. N.: Global aerosol climatology from the MODIS satellite sensors, Journal of Geophysical Research-Atmospheres, 113, D14s07, doi:10.1029/2007jd009661, 2008.

Richter, A., Burrows, J. P., Nu¨ß, H., Granier, C., and Niemeier, U.: Increase in tropospheric nitrogen dioxide over China observed from space, Nature, 437, 129-132, doi:10.1038/nature04092, 2005.

Rienecker, M. M., Suarez, M. J., Todling, R., Bacmeister, J., Takacs, L., Liu, H.-C., Gu, W., Sienkiewicz, M., Koster, R. D., Gelaro, R., Stajner, I., and Nielsen, E.: The GEOS-5 Data Assimilation System - Documentation of Versions 5.0.1, 9.1.0, and 5.2.0, NASA, 2008.

Sayer, A., Munchak, L., Hsu, N., Levy, R., Bettenhausen, C., and Jeong, M. J.: MODIS Collection 6 aerosol products: Comparison between Aqua's e‐Deep Blue, Dark Target, and “merged” data sets, and usage recommendations, 119, 13965–13989, doi:10.1002/2014JD022453, 2014.

Schaepman-Strub, G., Schaepman, M., Painter, T., Dangel, S., and Martonchik, J.: Reflectance quantities in optical remote sensing—Definitions and case studies, Remote Sensing of Environment, 103, 27-42, 2006.

Spurr, R.: LIDORT and VLIDORT: Linearized pseudo-spherical scalar and vector discrete ordinate radiative transfer models for use in remote sensing retrieval problems, Light Scattering Reviews, edited by: Kokhanovsky, A., Springer, 2008.

Stavrakou, T., Muller, J. F., Boersma, K. F., De Smedt, I., and van der A, R. J.: Assessing the distribution and growth rates of NOx emission sources by inverting a 10-year record of NO2 satellite columns, Geophysical Research Letters, 35, L10801, doi:10.1029/2008gl033521, 2008.

Streets, D. G., Bond, T. C., Carmichael, G. R., Fernandes, S. D., Fu, Q., He, D., Klimont, Z., Nelson, S. M., Tsai, N. Y., Wang, M. Q., Woo, J. H., and Yarber, K. F.: An inventory of gaseous and primary aerosol emissions in Asia in the year 2000, Journal of Geophysical Research-Atmospheres, 108, 8809, doi:10.1029/2002jd003093, 2003.

Turner, A., Henze, D., Martin, R., and Hakami, A.: The spatial extent of source influences on modeled column concentrations of short‐lived species, Geophys. Res. Lett., 39, L12806, doi:10.1029/2012GL051832,2012.

van der A, R. J., Eskes, H. J., Boersma, K. F., Noije, T. P. C. v., Roozendael, M. V., DeSmedt, I., Peters, D. H. M. U., and Meijer, E. W.: Trends, seasonal variability and dominant NOx source derived from a ten year record of NO2 measured from space, J. Geophys. Res., 113, doi:10.1029/2007JD009021, 2008.

van Donkelaar, A., Martin, R. V., Spurr, R. J. D., Drury, E., Remer, L. A., Levy, R. C., and Wang, J.: Optimal estimation for global ground-level fine particulate matter concentrations, Journal of Geophysical Research-Atmospheres, 118, 5621-5636, doi:10.1002/jgrd.50479, 2013.

Wang, L., Wang, Y., Xin, J., Li, Z., and Wang, X.: Assessment and comparison of three years of Terra and Aqua MODIS Aerosol Optical Depth Retrieval (C005) in Chinese terrestrial regions, Atmospheric Research, 97, 229-240, 2010.

Wang, L. L., Xin, J. Y., Wang, Y. S., Li, Z. Q., Liu, G. R., and Li, J.: Evaluation of the MODIS aerosol optical depth retrieval over different ecosystems in China during EAST-AIRE, Atmospheric Environment, 41, 7138-7149, doi:10.1016/j.atmosenv.2007.05.001, 2007.

Wang, Y., Xin, J., Li, Z., Wang, S., Wang, P., Hao, W. M., Nordgren, B. L., Chen, H., Wang, L., and Sun, Y.: Seasonal variations in aerosol optical properties over China, J. Geophys. Res., 116, D18209, doi:10.1029/2010JD015376,2011.

Winker, D. M., Vaughan, M. A., Omar, A., Hu, Y., Powell, K. A., Liu, Z., Hunt, W. H., and Young, S. A.: Overview of the CALIPSO mission and CALIOP data processing algorithms, Journal of Atmospheric and Oceanic Technology, 26, 2310-2323, 2009.

Xia, X. G., Li, Z. Q., Holben, B., Wang, P., Eck, T., Chen, H. B., Cribb, M., and Zhao, Y. X.: Aerosol optical properties and radiative effects in the Yangtze Delta region of China, Journal of Geophysical Research-Atmospheres, 112, doi:10.1029/2007jd008859, 2007.

Xin, J. Y., Wang, Y. S., Li, Z. Q., Wang, P. C., Hao, W. M., Nordgren, B. L., Wang, S. G., Liu, G. R., Wang, L. L., Wen, T. X., Sun, Y., and Hu, B.: Aerosol optical depth (AOD) and Angstrom exponent of aerosols observed by the Chinese Sun Hazemeter Network from August 2004 to September 2005, Journal of Geophysical Research-Atmospheres, 112, doi:10.1029/2006jd007075, 2007.

Yan, Y.-Y., Lin, J.-T., Kuang, Y., Yang, D.-W., and Zhang, L.: Tropospheric carbon monoxide over the Pacific during HIPPO: Two-way coupled simulation of GEOS-Chem and its multiple nested models, Atmos. Chem. Phys., 14, 12649-12663, doi:10.5194/acp-14-12649-2014, 2014.

Zhang, L., Jacob, D., Yue, X., Downey, N., Wood, D., and Blewitt, D.: Sources contributing to background surface ozone in the US Intermountain West, Atmospheric Chemistry and Physics, 14, 5295-5309, 2014.

Zhang, Q., He, K. B., and Huo, H.: Cleaning China's air, Nature, 484, 161-162, 2012.

Zhang, Q., Streets, D. G., Carmichael, G. R., He, K. B., Huo, H., Kannari, A., Klimont, Z., Park, I. S., Reddy, S., Fu, J. S., Chen, D., Duan, L., Lei, Y., Wang, L. T., and Yao, Z. L.: Asian emissions in 2006 for the NASA INTEX-B mission, Atmospheric Chemistry and Physics, 9, 5131-5153, 2009.

Zhao, C., and Wang, Y. H.: Assimilated inversion of NOx emissions over east Asia using OMI NO2 column measurements, Geophysical Research Letters, 36, L06805, doi:10.1029/2008gl037123, 2009.

Zhao, Y., Duan, L., Xing, J., Larssen, T., Nielsen, C. P., and Hao, J. M.: Soil Acidification in China: Is Controlling SO2 Emissions Enough?, Environmental Science & Technology, 43, 8021-8026, doi:10.1021/es901430n, 2009.

Zhou, Y., Brunner, D., Spurr, R. J. D., Boersma, K. F., Sneep, M., Popp, C., and Buchmann, B.: Accounting for surface reflectance anisotropy in satellite retrievals of tropospheric NO2, Atmospheric Measurement Techniques, 3, 1185-1203, doi:10.5194/amt-3-1185-2010, 2010.

Table 1. Key tools and parameters used in POMINO and associated cloud retrievals

	POMINO NO_2 retrieval	Cloud (O_2-O_2)
AMF package	AMFv6; OpenMP parallelization	Same
RTM	LIDORT v3.6 (un-polarized, curved atmosphere); OpenMP parallelization	Same
Calculation for individual pixels	Pixel-specific radiative transfer modeling; no look-up table	Same
Surface reflectance	Land: BRDF at 440 nm, MCD43C2 Collection 5 (0.05 º); Oceanic: OMLER v3 albedo	Same
Surface pressure	GEOS-5 [a]; adjusted by elevation [b]	Same
Cloud fraction and cloud pressure	Derived here	–

Aerosol optical parameters	GEOS-Chem v9-02 [a]; at 438 nm; Model AOD is adjusted by MODIS/Aqua AOD [c]	Similar, but at 475 nm [c]
Vertical profile of NO_2	GEOS-Chem v9-02 [a,d]	–
Vertical profiles of pressure and temperature	GEOS-5 [a,d]	Same

[a] Resolution: 0.667 ° long. x 0.5 ° lat. horizontally with 47 layers vertically and ~ 10 layers below 1.5 km.

[b] Elevation information are from the GMTED2010 dataset at 30 arc-seconds (http://topotools.cr.usgs.gov/GMTED_viewer/)

[c] See Sect. 2.3 for details.

[d] The pressure levels are re-calculated according to the elevation-adjusted surface pressure; while the volume mixing ratios of NO_2 are not changed in individual layers (Zhou et al., 2009).

Table 2. Retrievals of clouds and NO_2 with different approaches *

	REF = POMINO	SRF	AER	S_A	DOM
Surface Reflectance	MCD43C2 BRDF	OMLER v3 albedo	MCD43C2 BRDF	OMLER v3 albedo	OMLER v1 albedo
Aerosol treatment	Explicit	Explicit	Implicit	Implicit	Implicit

* Retrieval procedures and parameters not mentioned here are the same for cases REF, SRF, AER and S_A. Case DOM is adopted from DOMINO v2.

Table 3. *a priori*, top-down and *a posteriori* emissions of NO_x *

	China (80 °E–130 °E, 20 °N–53 °N)					East China (101.25 °E–126.25 °E, 20 °N–46 °N)				
	REF	SRF	AER	S_A	DOM	REF	SRF	AER	S_A	DOM
a priori	9.78	9.78	9.78	9.78	9.78	9.11	9.11	9.11	9.11	9.11
With OMI data sampled at valid pixels specific to each case										
Top-down	8.50	8.20	8.63	8.21	8.75	7.92	7.65	8.03	7.65	8.19
a posteriori	9.05	8.88	9.12	8.88	9.19	8.43	8.27	8.49	8.27	8.58
With OMI data sampled at valid pixels by REF										
Top-down	8.50	8.23	8.91	8.53	8.80	7.92	7.68	8.33	7.97	8.27
a posteriori	9.05	8.90	9.28	9.06	9.22	8.43	8.29	8.66	8.46	8.63

* Units: TgN yr^{-1}

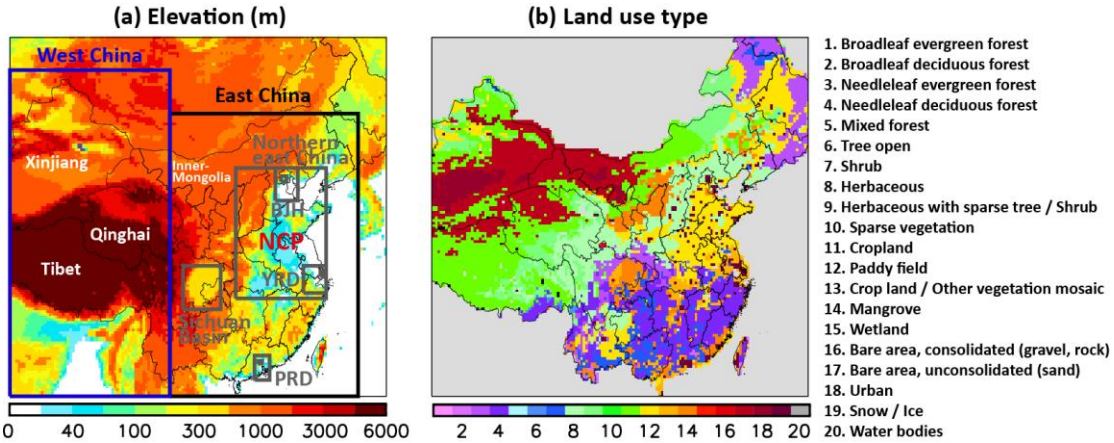

Fig. 1. (a) USGS GMTED2010 surface elevation and (b) ISCGM GLCNMO land use types mapped to a 0.25 ° long. x 0.25 ° lat. grid. Provincial boundaries of China are shown. Urban land use type is highlighted in (b), such that a grid cell is designated as 'urban' if at least 5% of its land is covered by urban areas. Also indicated in (a) are provinces (in white) and regions (in various colors) mentioned in the text. East China: 101.25 °E–126.25 °E, 20 °N–46 °N; West China: 80 °E–101.25 °E, 20 °N–50 °N; northern east China: 110 °E–122 °E, 29 °N–41 °N; Sichuan Basin: 103 °E–108 °E, 28 °N–32 °N; Beijing-Tianjin-Hebei (BTH): 115.25 °E–118.25 °E, 38 °N–41 °N; urban Beijing:

116 °E–116.75 °E, 39.75 °N–40.25 °N; Yangtze River Delta (YRD): 119 °E–122 °E, 29.5 °N–32 °N; urban Shanghai: 121.25 °E–121.75 °E, 31 °N–31.5 °N; Pearl River Delta (PRD): 112.5 °E–114.5 °E, 21.5 °N–23.75 °N; and urban Guangzhou: 113 °E–113.5 °E, 23 °N–23.25 °N. Urban Beijing, urban Shanghai, and urban Guangzhou are inside BTH, YRD and PRD, respectively. The North China Plain (NCP) indicated in red represents the low-elevation (< 300 m) areas of northern east China.

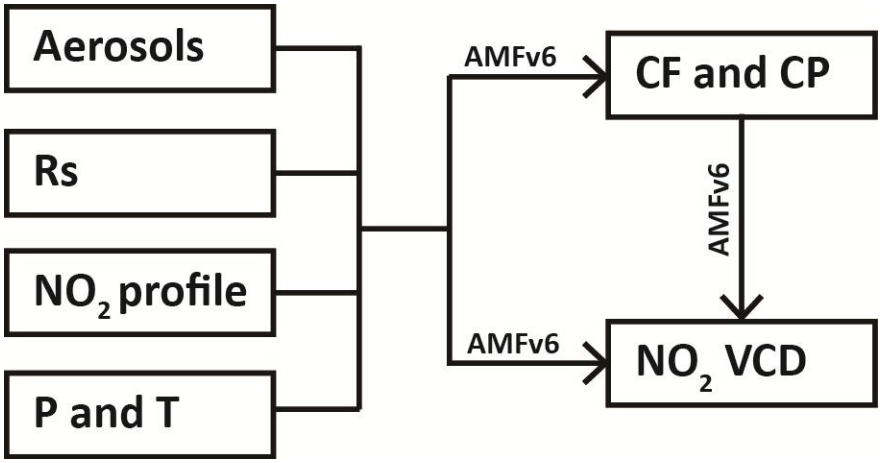

Fig. 2. A diagram to illustrate our reference retrieval (case REF, representing our POMINO product). Here Rs is surface reflectance, P is air pressure, and T is air temperature. See Sect. 2.2 and Table 1 for detailed descriptions of our retrieval approach and parameters.

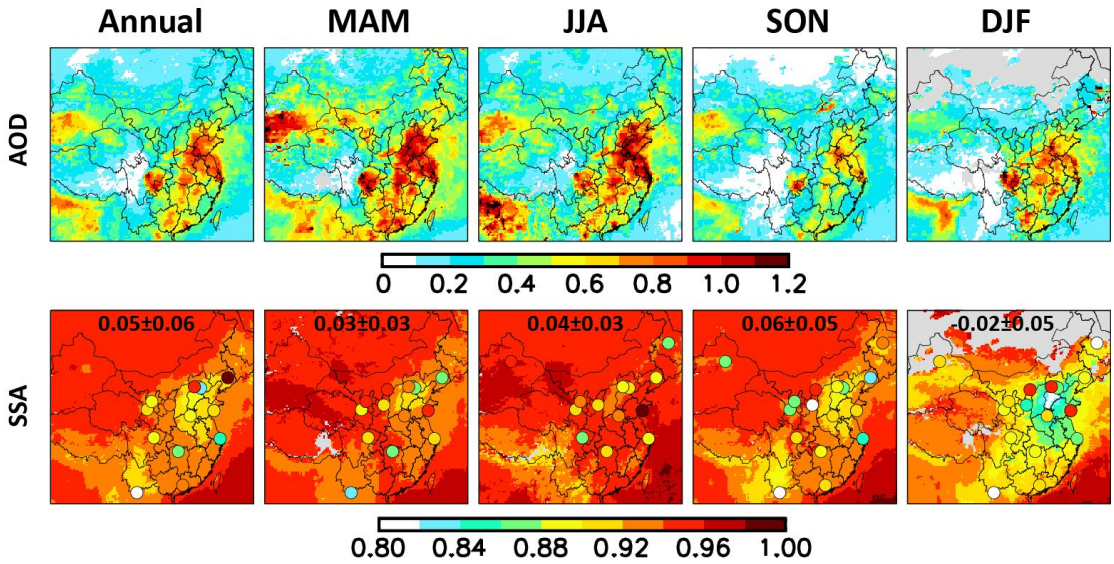

Fig. 3. AOD and SSA at annual and seasonal scales. Provincial boundaries of China are shown. Data are sampled from valid pixels of case REF. AOD values exceeding a value of 1.2 are shown in black. Missing values are shown in grey. Filled circles in the second row indicate the SSA estimates for 2005 with AOD > 0.4 by Lee et al. (2007). The embedded numbers are our SSA values minus Lee et al. (± 1 standard deviation); our data are sampled at grid cells covering their sites.

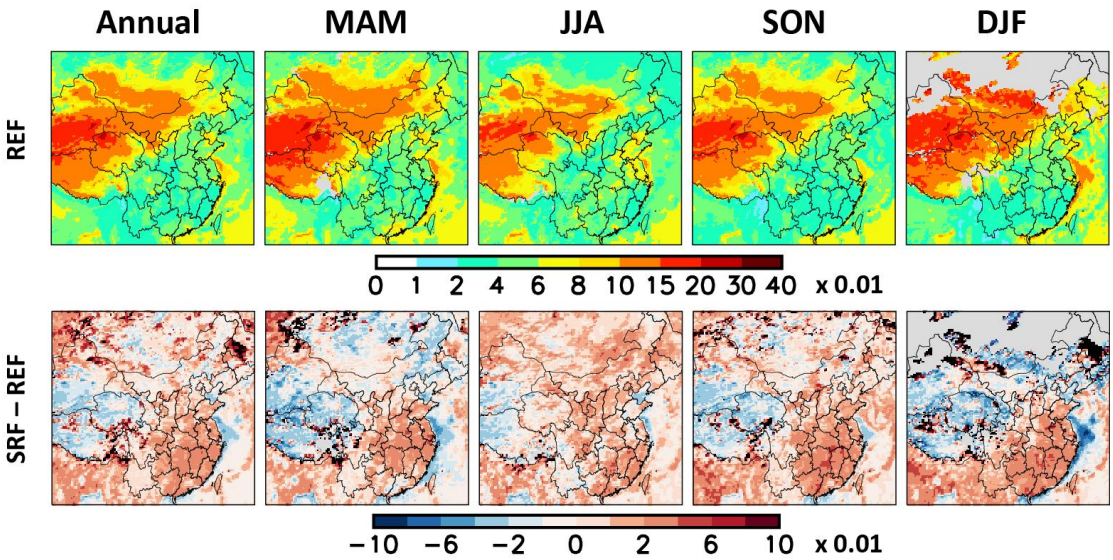

Fig. 4. (First row) Surface reflectance in case REF = POMINO (MODIS BRF data) at annual and seasonal scales. (Second row) Surface reflectance in case SRF (OMLER v1 albedo) minus reflectance in case REF (MODIS BRF). Provincial boundaries of China are shown. Data are sampled from valid pixels of case REF. Values outside the upper (lower) bound of color intervals are shown in black (purple). Missing values are shown in grey. Color intervals are nonlinear to better present the data range; an interval without labeling represents the mean of adjacent two intervals.

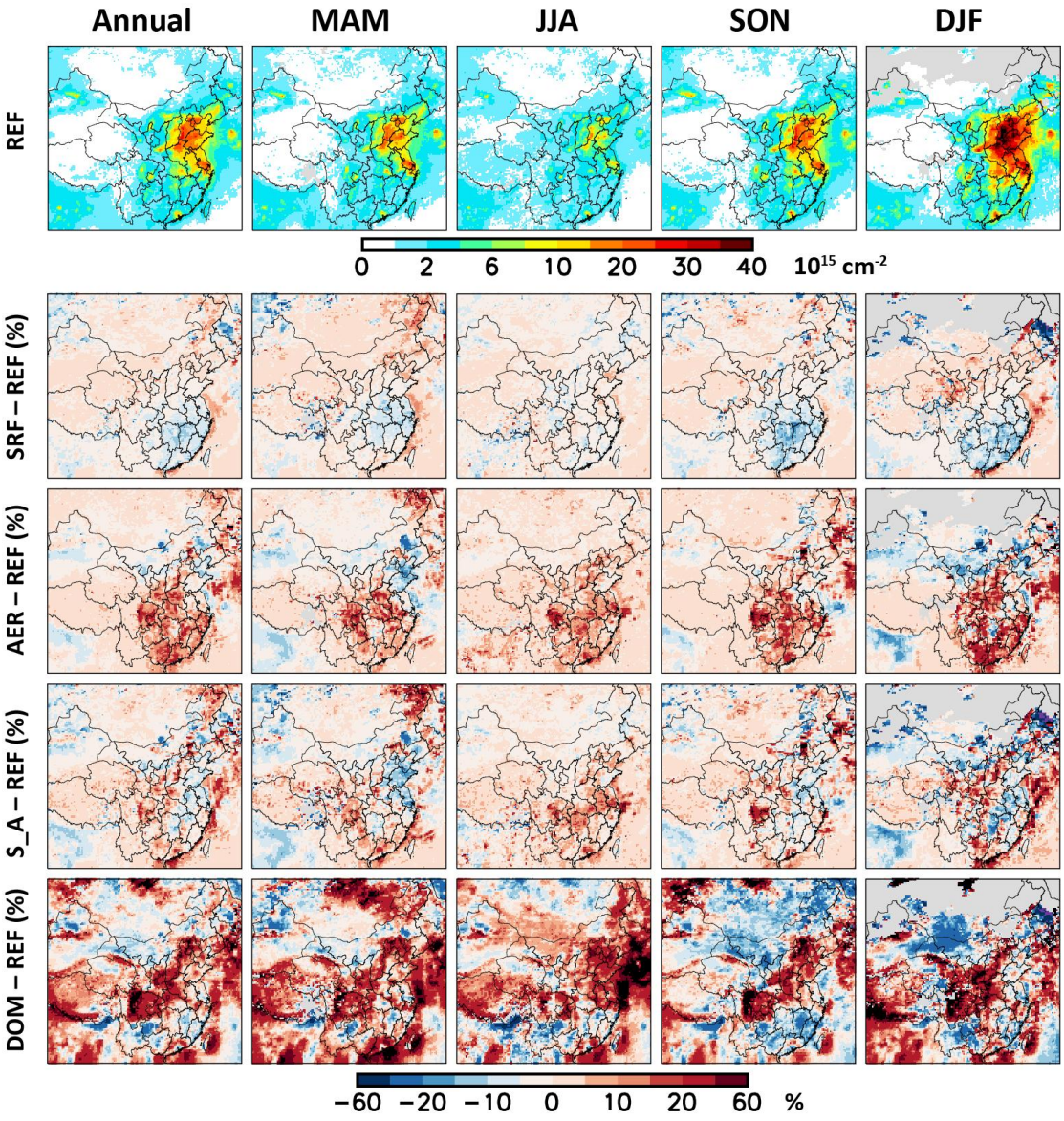

Fig. 5. (First row) Tropospheric NO_2 VCDs retrieved from case REF at annual and seasonal scales. (Second–fifth rows) changes in NO_2 VCDs from case REF to other cases as a percentage fraction of case REF. Provincial boundaries of China are shown. Data are sampled from valid pixels of case REF. Values outside the upper (lower) bound of color intervals are shown in black (purple). Missing values are shown in grey. Color intervals are nonlinear to better present the data range; an interval without labeling represents the mean of adjacent two intervals.

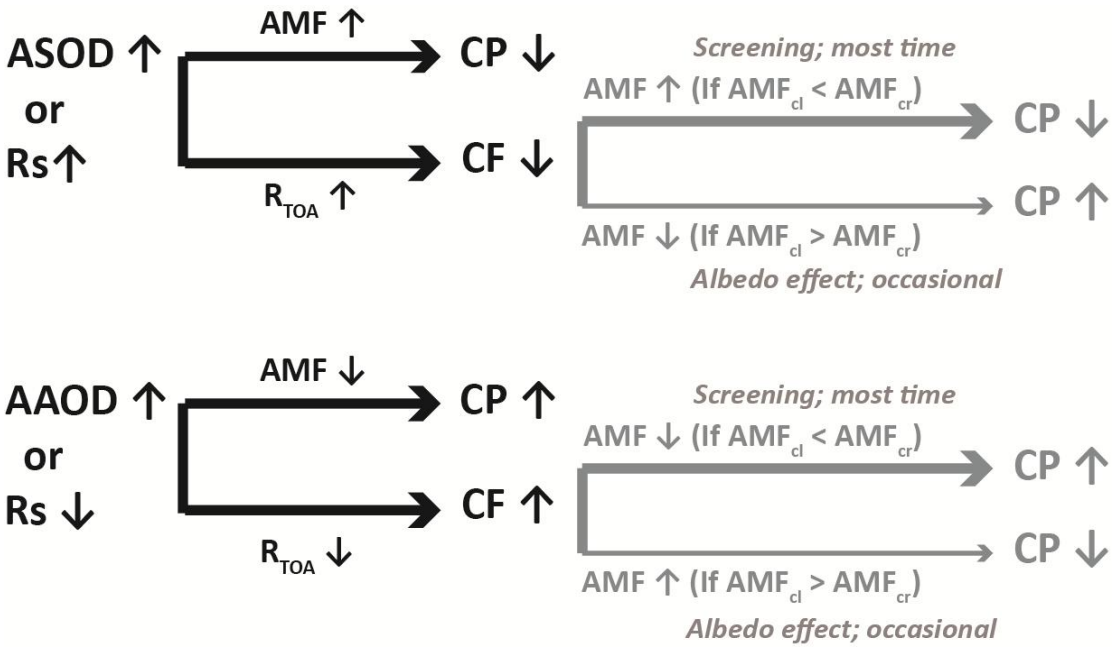

Fig. 6. A diagram of how changes in surface reflectance (Rs), aerosol scattering (ASOD) and aerosol absorption (AAOD) affect the retrievals of CF and CP in the O_2-O_2 algorithm. Grey colors illustrate the indirect influence of CF changes on the CP; the influence depends on the "screening" or "albedo" effects of clouds on radiation. Thin grey lines indicate that the "albedo" effect of clouds is occasional. The figure is updated from Fig. 5 of Lin et al. (2014b).

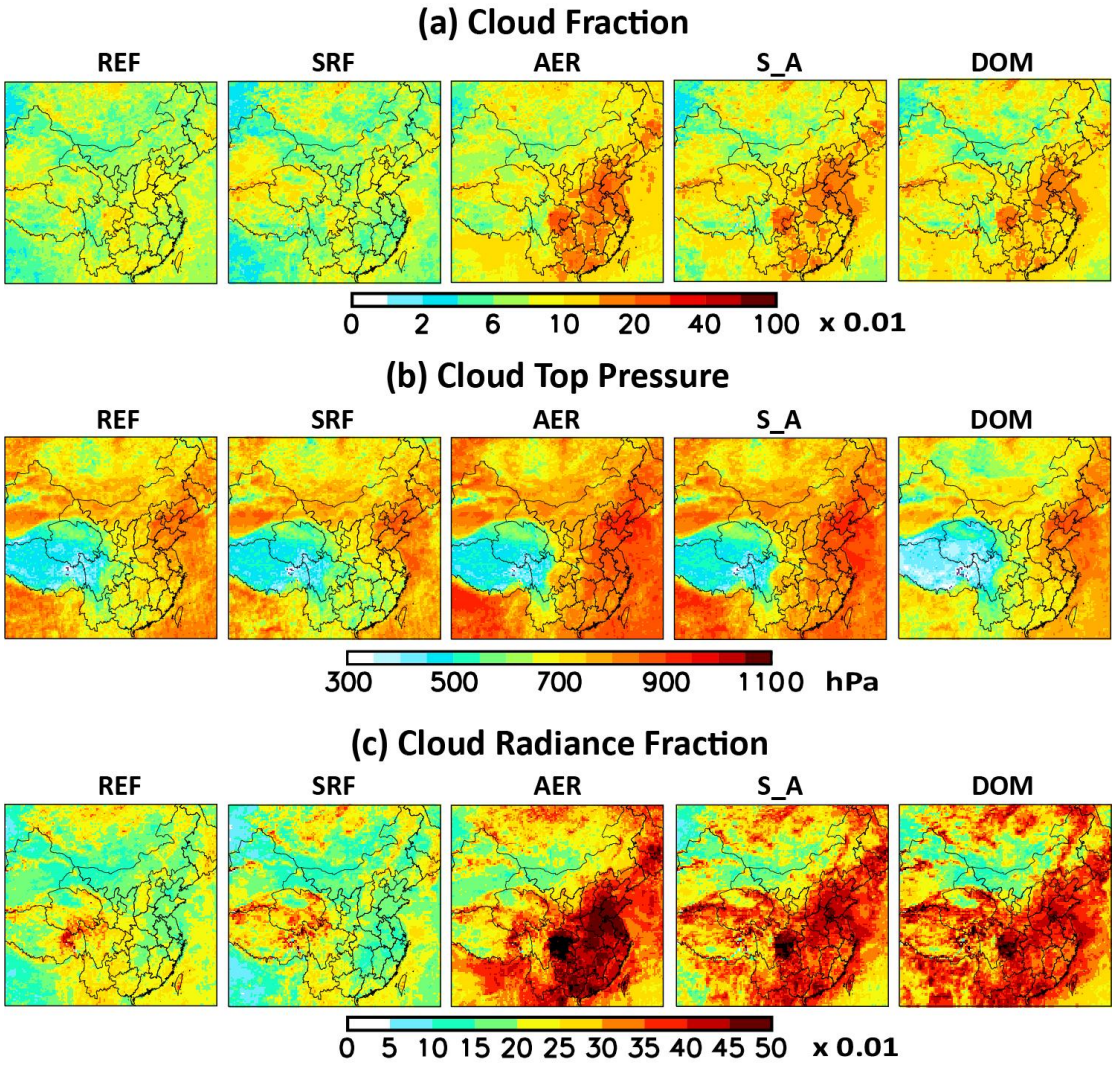

Fig. 7. Annual mean (a) cloud fraction, (b) cloud top pressure and (c) cloud radiance fraction retrieved via different approaches. Provincial boundaries of China are shown. Data are sampled from valid pixels of case REF. Values outside the upper (lower) bound of color intervals are shown in black (purple). Missing values are shown in grey. Color intervals in (a) are nonlinear to better present the data range; an interval without labeling represents the mean of adjacent two intervals.

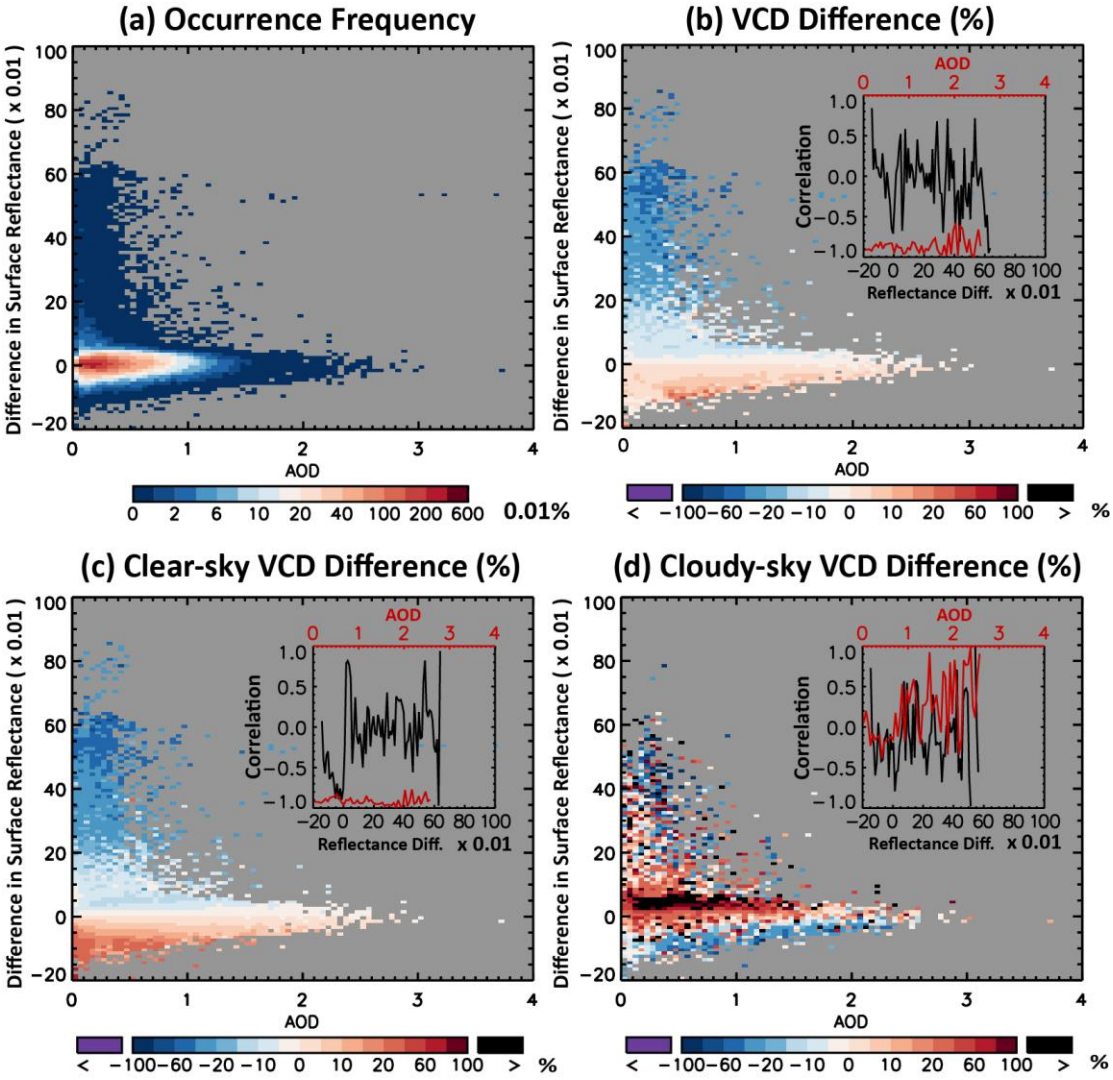

Fig. 8. (a) Frequency of occurrence from all months and grid cells for each bin of AOD (x-axis, bin size = 0.05) and surface reflectance difference (OMI albedo in case SRF minus MODIS BRF in case REF, y-axis, bin size = 0.01). Data are sampled from valid pixels of case REF. (b) Percentage changes in NO_2 VCDs from case REF to SRF averaged over all data in each bin of AOD and surface reflectance difference; also embedded are the correlation between percentage VCD changes and AOD values as a function of surface reflectance differences (black line) and between VCD changes and surface reflectance differences as a function of AOD values (red line). Similar panels are drawn for (c) clear-sky VCDs and (d) cloudy-sky VCDs.

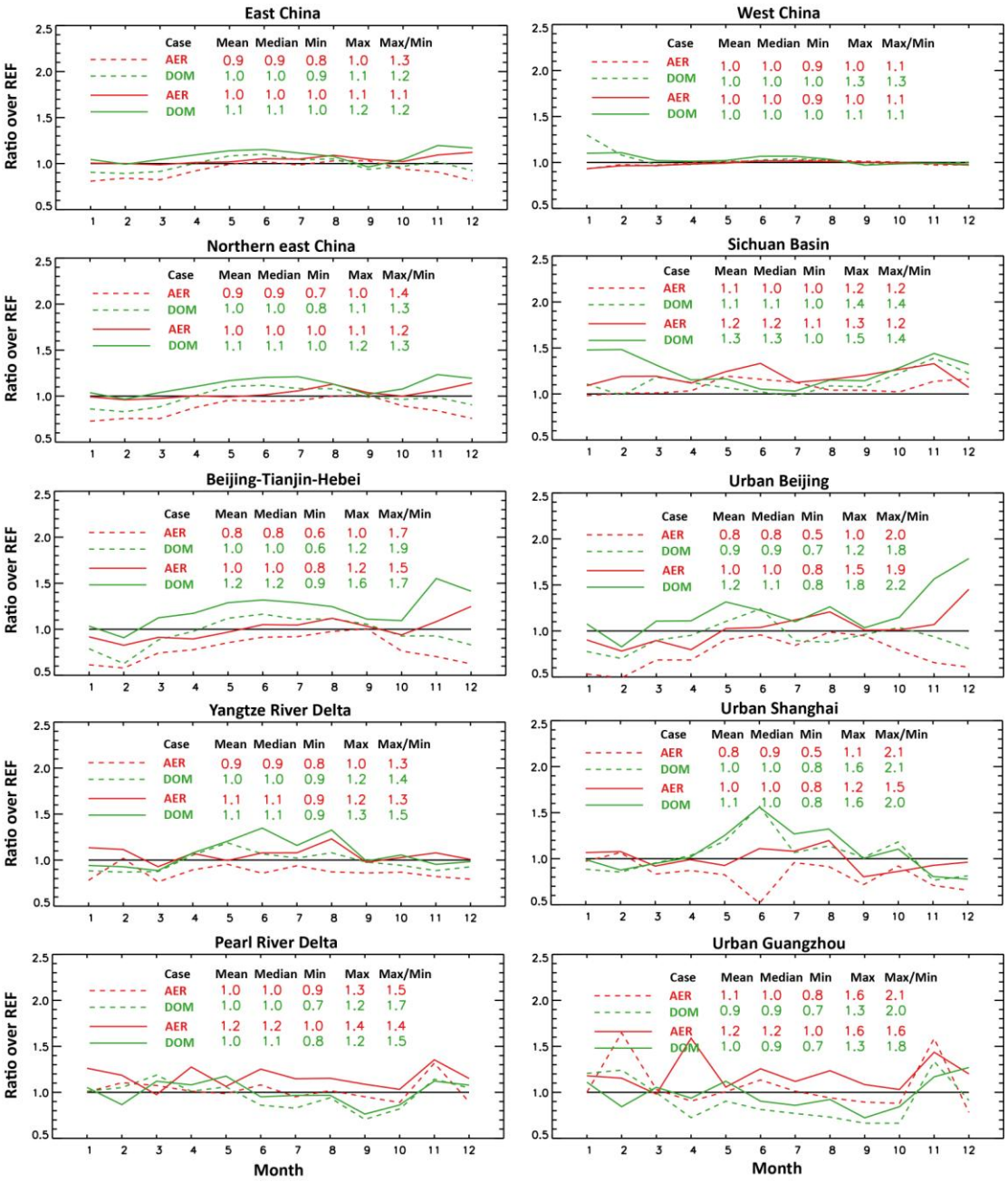

Fig. 9. Ratios of cases AER and DOM to case REF for regional mean NO_2 VCDs in each month of 2012. Regions are defined in Fig. 1a. For cases AER and DOM, data can be sampled from pixels valid in respective retrieval approaches (dotted lines) or valid in case REF (solid lines). Also shown are some statistical quantities.

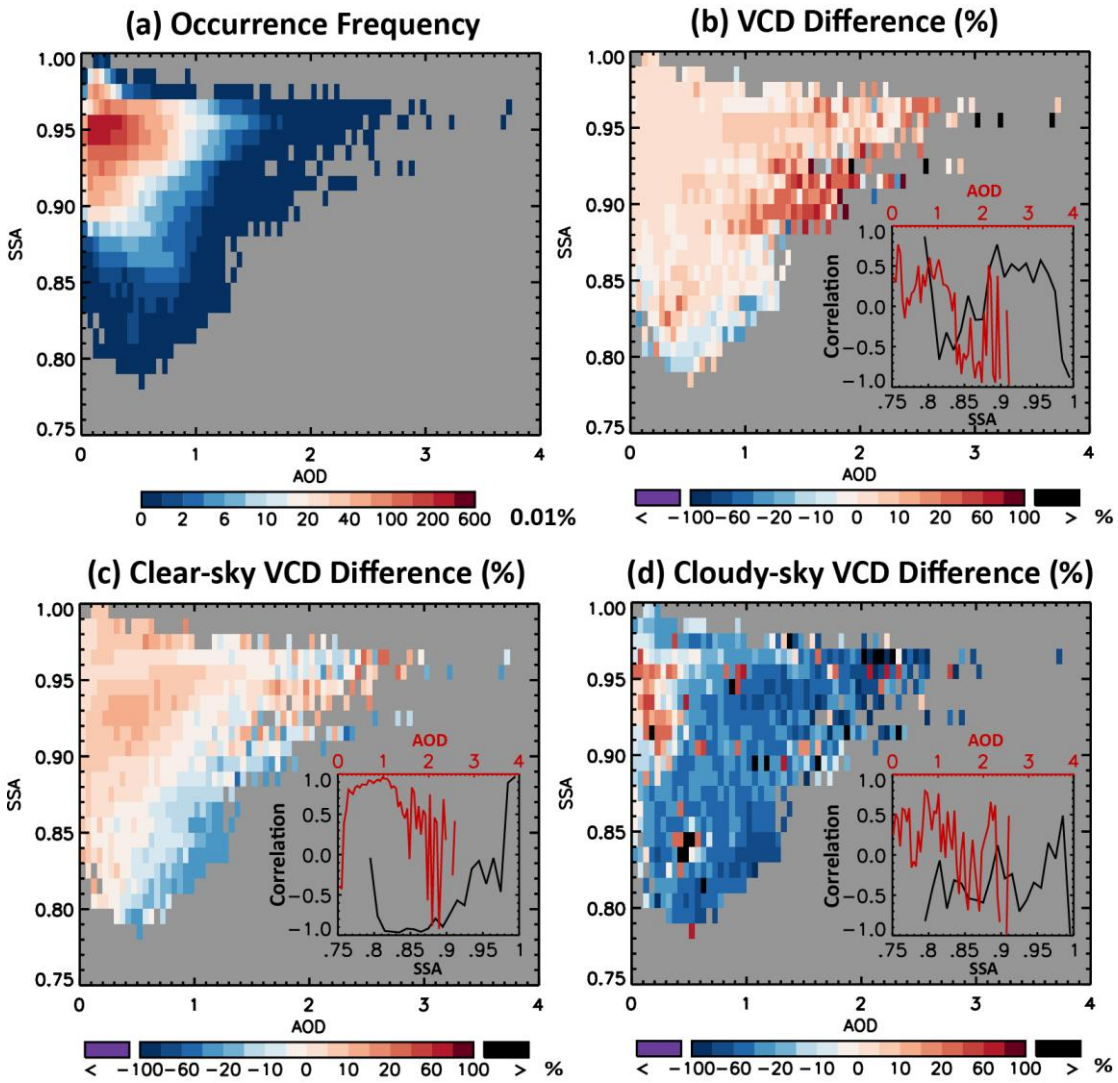

Fig. 10. (a) Frequency of occurrence from all months and grid cells for each bin of AOD (x-axis, bin size = 0.05) and SSA (y-axis, bin size = 0.01). Data are sampled from valid pixels of case REF. (b) Percentage changes in NO_2 VCDs from case REF to SRF averaged over all data in each bin of AOD and SSA; also embedded are the correlation between percentage VCD changes and AOD values as a function of SSA values (black line) and between VCD changes and SSA values as a function of AOD values (red line). Similar panels are drawn for (c) clear-sky VCDs and (d) cloudy-sky VCDs.

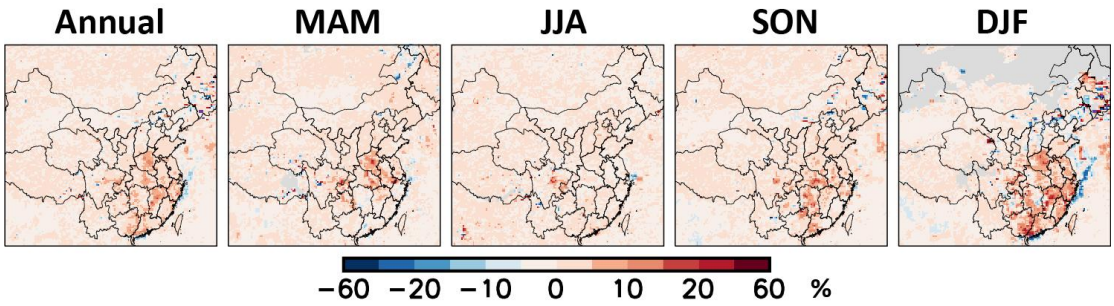

Fig. 11. Differences in NO_2 VCDs between (SRF – REF) + (AER – REF) and (S_A – REF) as a percentage fraction of REF. Provincial boundaries of China are shown. Data are sampled from valid pixels of case REF. Values outside the upper (lower) bound of color intervals are shown in black (purple). Missing values are shown in grey. Color intervals are nonlinear to better present the data range; an interval without labeling represents the mean of adjacent two intervals.

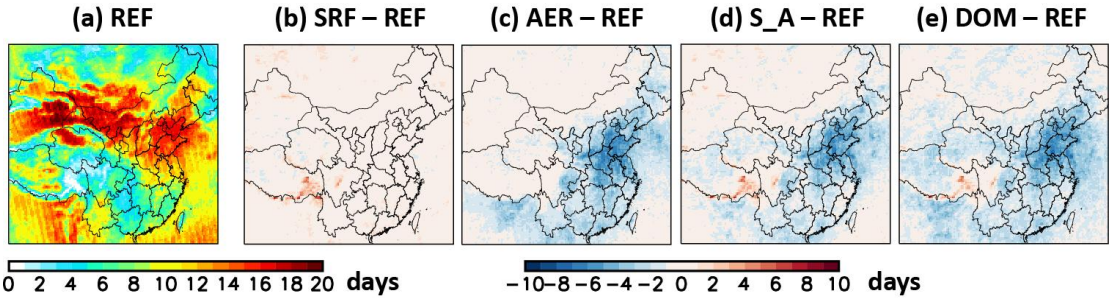

Fig. 12. (a) Number of days per month of 2012 with valid pixels in case REF on a 0.25 °long. x 0.25 °lat. grid. (b) Changes in the number of days per month with valid pixels from REF to other cases. Provincial boundaries of China are shown.

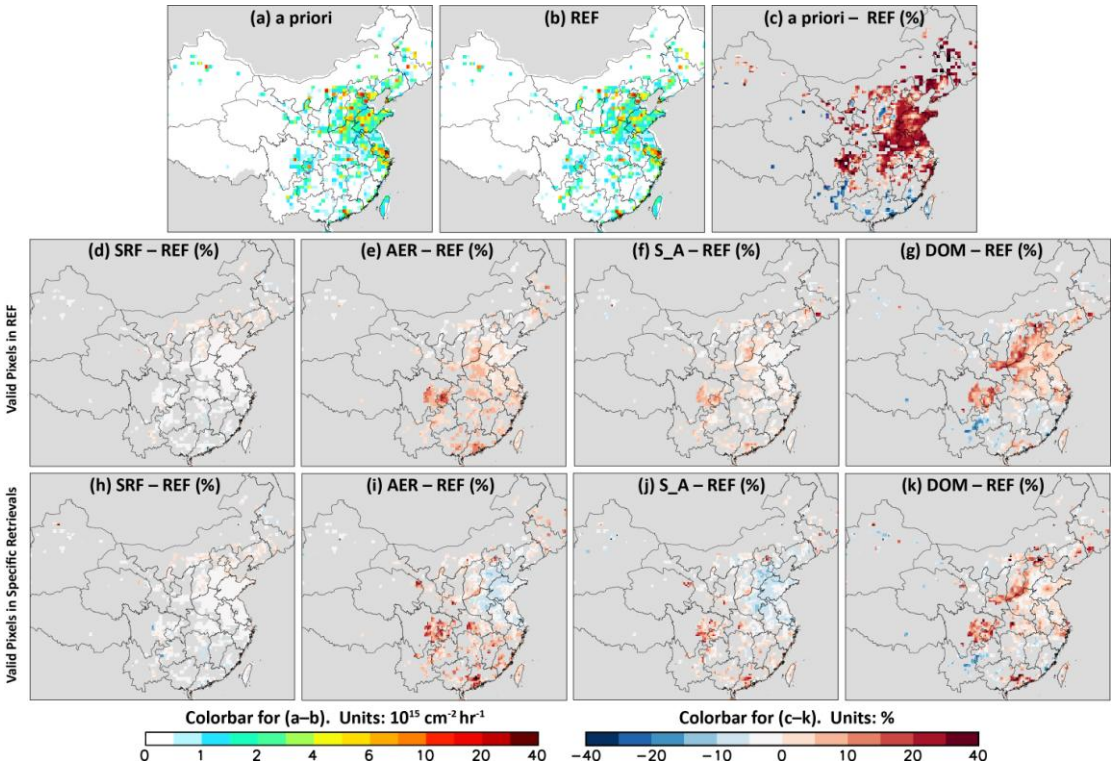

Fig. 13. (a) The *a priori* anthropogenic emissions of NO_x on a 0.25 °long. x 0.25 °lat. grid. (b) The *a posteriori* emissions constrained by case REF. (c) Differences between *a priori* and REF as a percentage fraction of REF. (d–g) Changes in *a posteriori* emissions from REF to other cases as a percentage fraction of REF; OMI pixels are selected only when valid in case REF. (h–k) are similar to (d–g) but with respect to pixels valid in individual retrieval approaches. In (c–k), areas with emissions below 0.5 x 10^{15} cm^{-2} hr^{-1} are masked. Provincial boundaries of China are shown. Values outside the upper (lower) bound of color intervals are shown in black (purple). Color intervals are nonlinear to better present the data range; an interval without labeling represents the mean of adjacent two intervals.

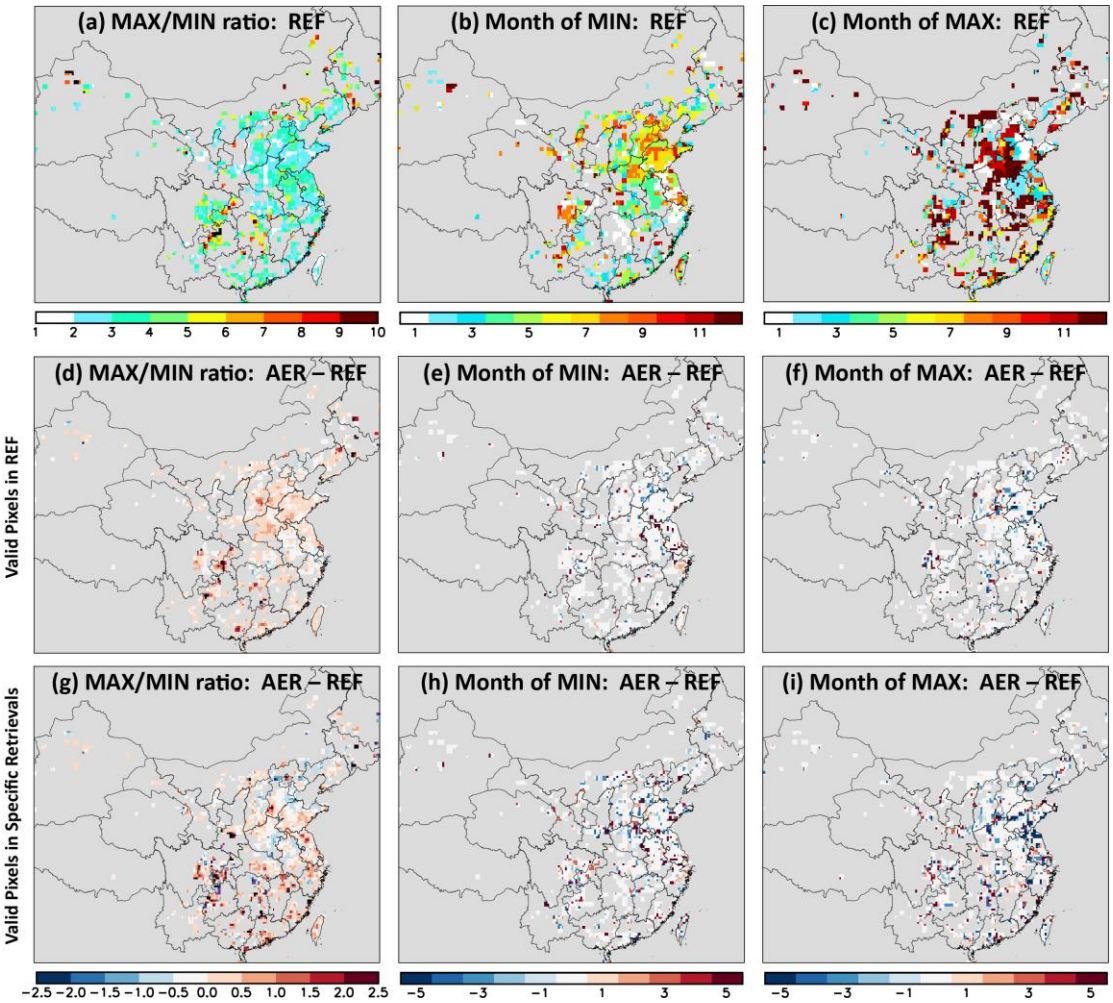

Fig. 14. (a) The maximum to minimum ratio for monthly *a posteriori* anthropogenic emissions in case REF, and the months of (b) minimum and (c) maximum emissions. (d–f) Differences between case AER and REF; OMI pixels are selected only when valid in case REF. (g–i) are similar to (d–f) but with respect to pixels valid in individual retrieval cases. Provincial boundaries of China are shown. Values outside the upper (lower) bound of color intervals are shown in black (purple). In (d)–(i), areas with emissions below 0.5 x 10^{15} cm^{-2} hr^{-1} are masked. In (e), (f), (h) and (i), the month proceeds in loop, i.e., November (January) is one month behind (ahead of) December.

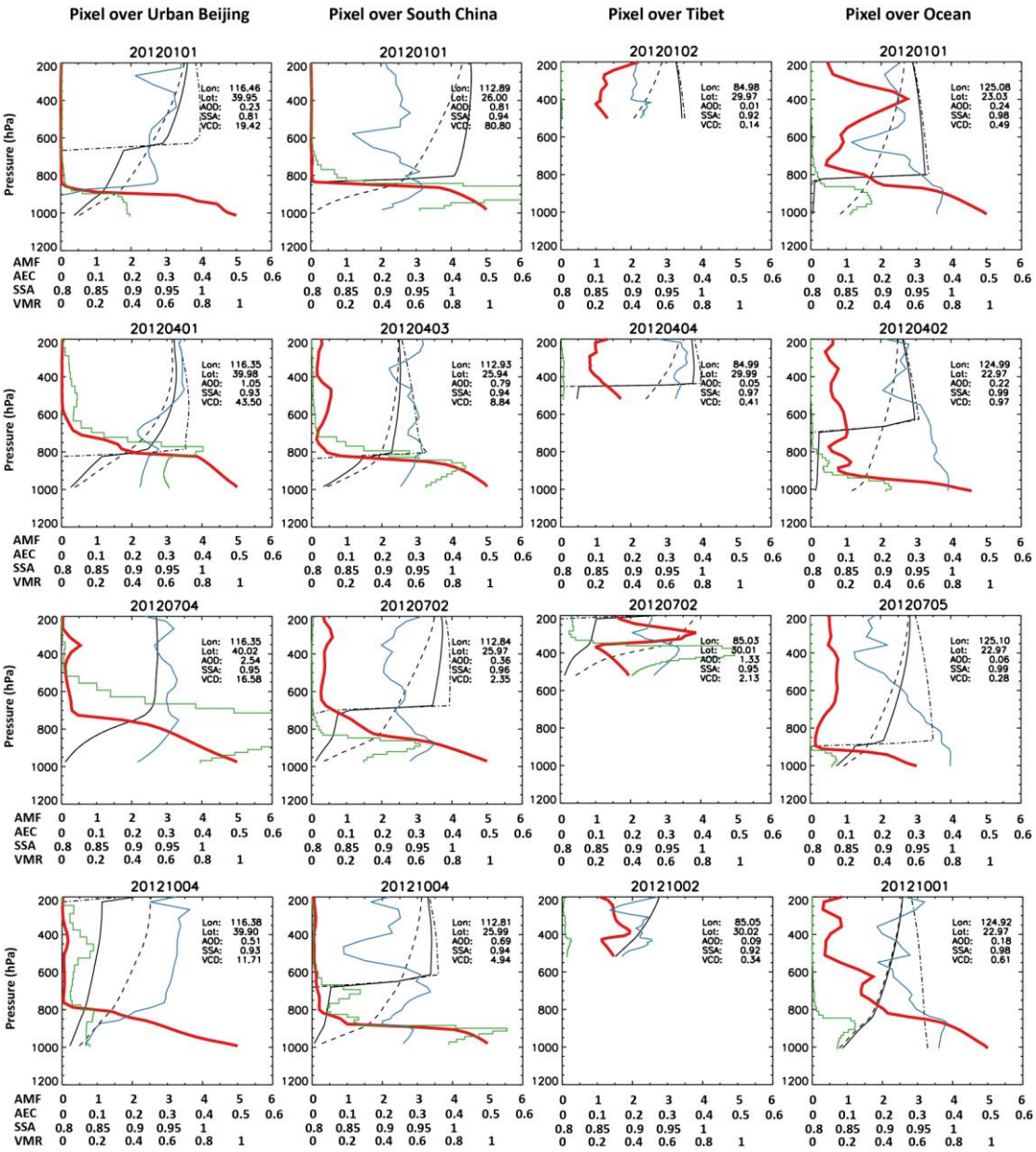

Fig. A1. Vertical profiles of NO_2 volume mixing ratios (VMRs, thick red lines), aerosol extinction coefficients (AECs, green lines), SSA (blue lines), AMFs (black lines), clear-sky AMFs (black dashed lines), and cloudy-sky AMFs (black dotted dashed lines) at the beginning of January, April, July and October at representative pixels in four areas: urban Beijing, south China, Tibet, and the oceans. The VMRs are normalized to the maximum VMR of the vertical profile. Embedded in each panel are longitude, latitude, AOD, SSA and retrieved NO_2 VCDs (in 10^{15} cm^{-2}). Here, '20120101' in the title of the top-left panel means January 1st, 2012, and so on.

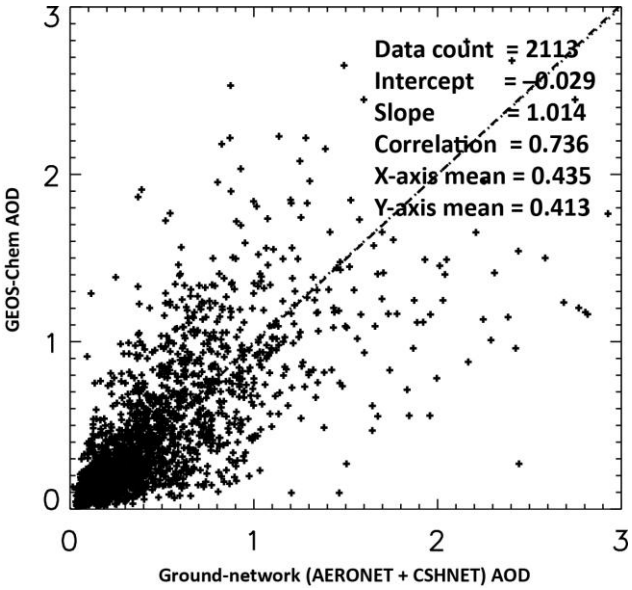

Fig. A2. Scatter plot of AOD at 550 nm from GEOS-Chem simulations versus ground networks (AERONET + CSHNET). Model AOD have been adjusted by MODIS AOD on a monthly basis (see Appendix B).